POLITECNICO
MILANO 1863

SCUOLA DI INGEGNERIA INDUSTRIALE
E DELL'INFORMAZIONE

Selective Volume Illumination Microscopy for Compressed Sensing of time lapse series

TESI DI LAUREA MAGISTRALE IN
ENGINEERING PHYSICS – INGEGNERIA FISICA

Author: **Marco Tobia Vitali**

Student ID: 964030
Advisor: Prof. Andrea Bassi
Co-advisors: Prof. Alessia Candeo, Gianmaria Calisesi Ph.D.
Academic Year: 2021-22

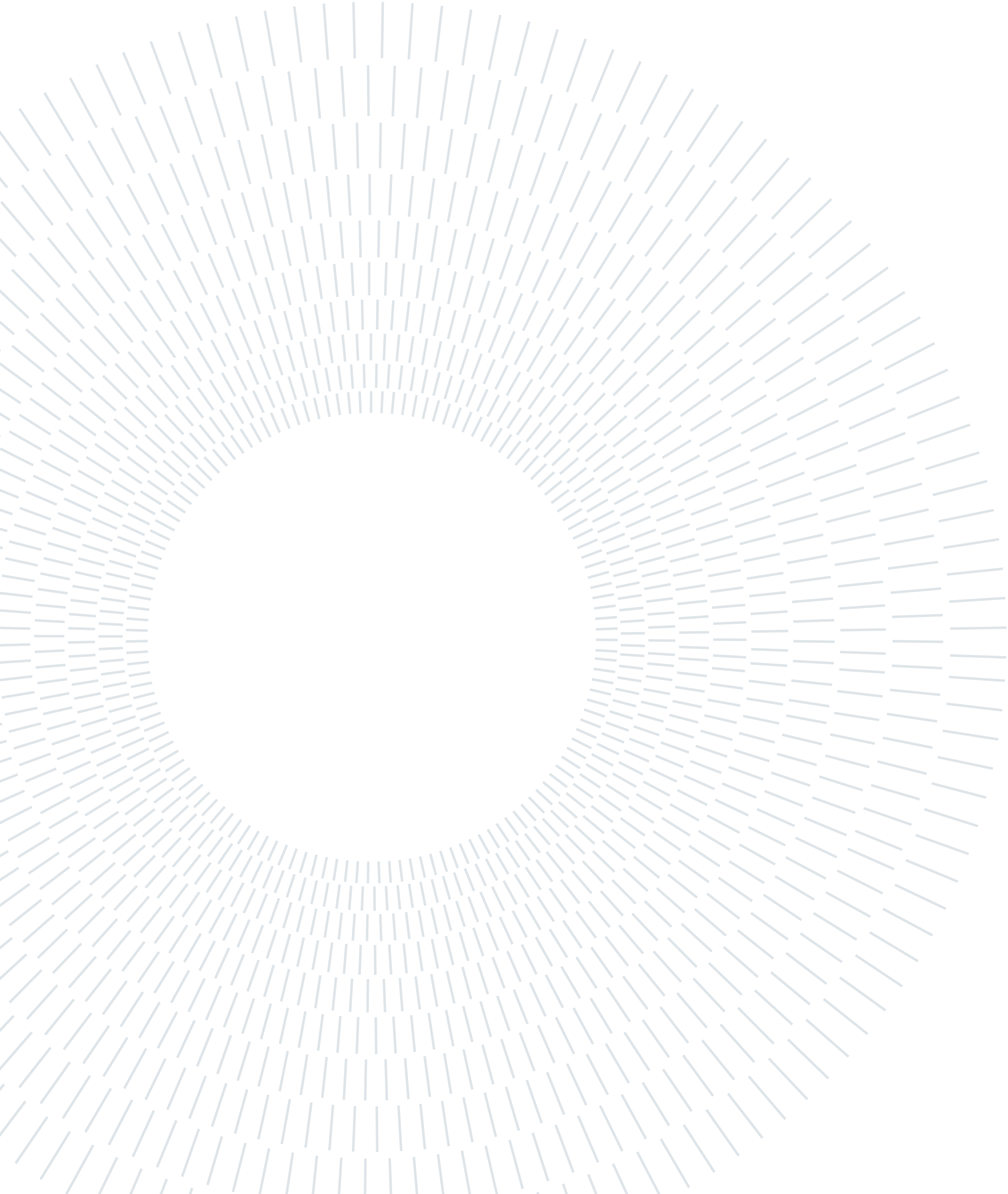

Abstract

We built and tested a fluorescence microscope that combines Light Sheet Fluorescence Microscopy with Compressed Sensing for the 4D imaging of live biological samples. Our aim was to achieve temporal resolutions in the order of 20 ms using common and relatively inexpensive optical components. We used a Digital Micromirror Device to modulate the illumination across the sample volume. High radiance and incoherent illumination was produced by coupling a diode laser to a multimode fiber. We employed scrambled Hadamard patterns to test the system on the zebrafish heart. We performed experiments without compressed sensing and we optimized the acquisition time of a single volume (with 16 planes in the axial direction) down to 41.41 ms. This time was close enough to our target temporal resolution to make Low Rank regularization a viable option. To test acquisition and reconstruction requirements with noisy data, we applied different regularization types to retrospectively down-sampled data sets. We found that Low Rank regularization was necessary to obtain good results when reconstructing time lapses that have few measurements for each time point.

Keywords: Fluorescent Microscopy, Selective Volume Illumination Microscopy, Low Rank Compressed Sensing, Digital Micromirror Device, Zebrafish Heart

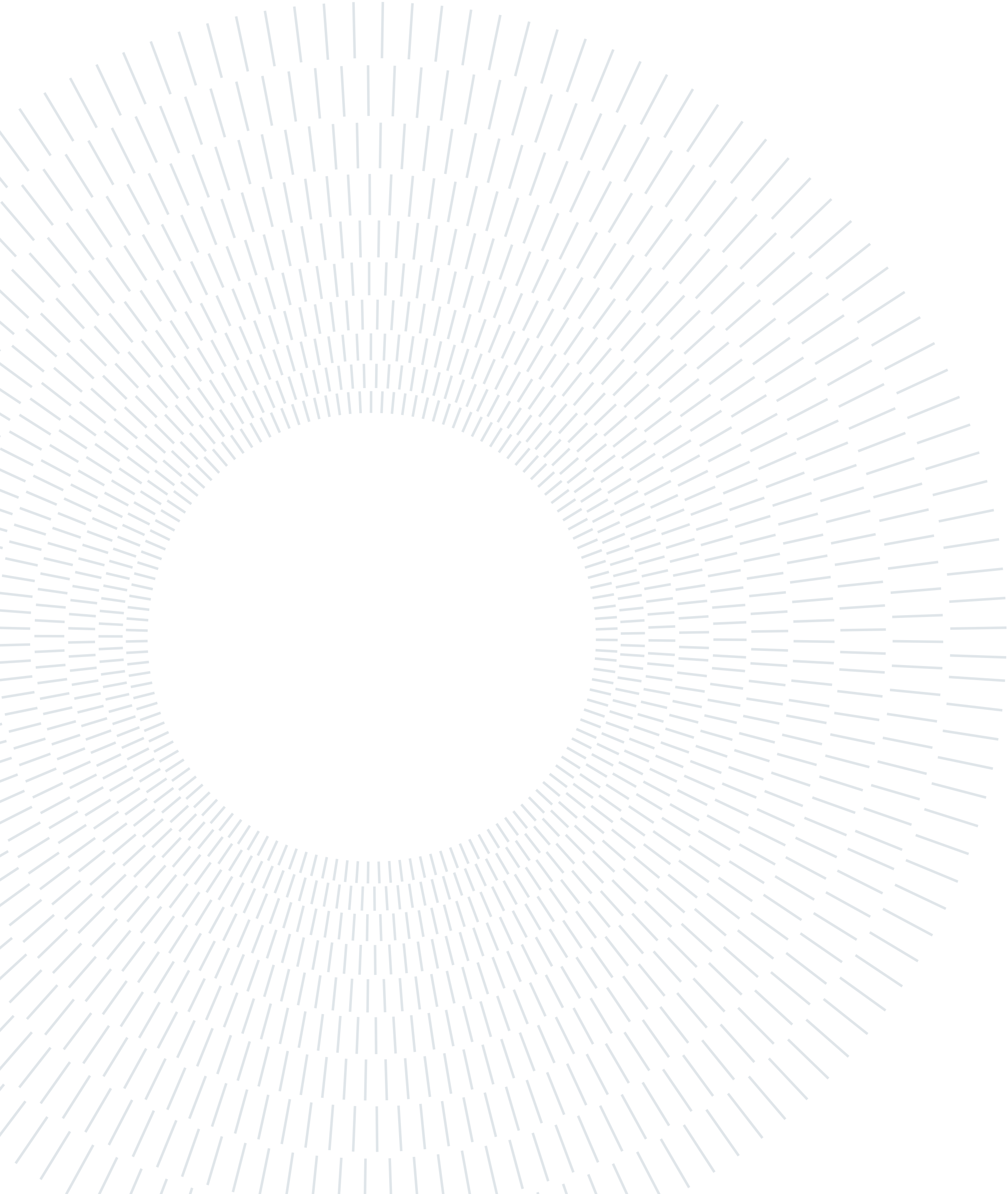

Abstract in lingua italiana

Abbiamo costruito e provato sperimentalmente un microscopio a fluorescenza che combina la *Light Sheet Fluorescence Microscopy* con il *Compressed Sensing* per ottenere immagini 4D di campioni biologici in vivo. Il nostro obiettivo era di raggiungere una risoluzione temporale nell'ordine di 20 ms usando componenti ottici comuni e relativamente economici. Abbiamo usato un *Digital Micromirror Device* per modulare l'illuminazione sul campione e creato un'illuminazione incoerente ad elevata radianza accoppiando un laser a diodo con una fibra ottica multimodo. Usando permutazioni casuali dei pattern di Hadamard, abbiamo collaudato il microscopio a fluorescenza misurando in vivo il movimento del cuore dello Zebrafish. Esperimenti senza il Compressed Sensing hanno portato a 41.41 ms il tempo di acquisizione di volumi con 16 piani in direzione assiale. Questo tempo di acquisizione era abbastanza vicino al nostro obiettivo da rendere possibile la regolarizzazione con Low Rank. Per testare i requisiti di acquisizione e di ricostruzione abbiamo applicato diverse regolarizzazioni a data set compressi solo in fase di analisi. Abbiamo visto che la regolarizzazione Low Rank era necessaria per ottenere buone ricostruzioni di serie temporali con poche misure per ciascun volume.

Parole chiave: Microscopia a fluorescenza, Selective Volume Illumination Microscopy, Low Rank Compressed Sensing, Digital Micromirror Device, cuore di Zebrafish

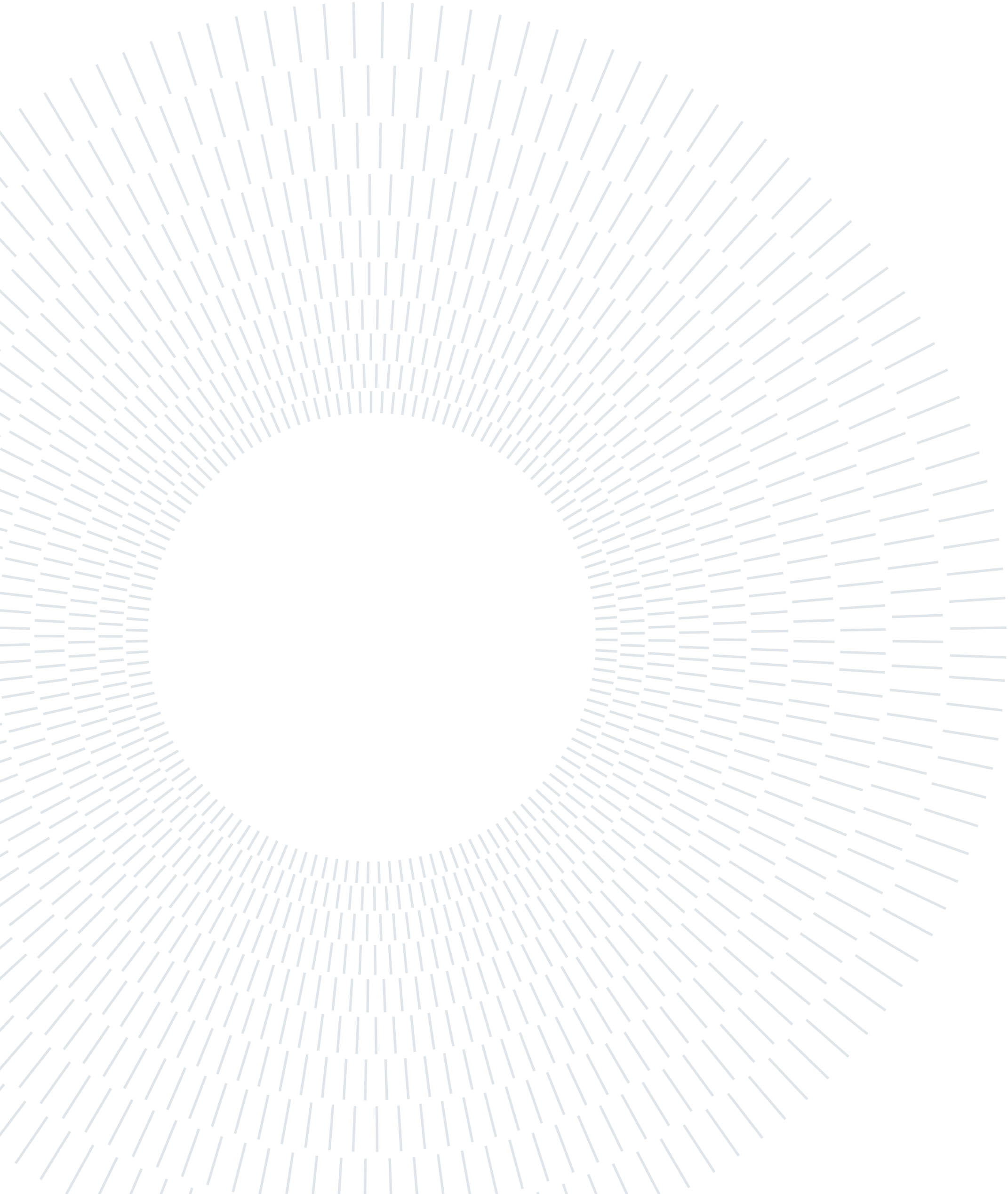

Contents

Introduction

Fluorescence Microscopy is extensively used in experimental biology because of its high sensitivity and specificity. Moreover, Fluorescence microscopy allows to image live samples that range from single molecules to whole organisms.

A microscope designed to acquire volumetric (i.e., three dimensional) and time lapse images of a live and dynamic sample must take into close consideration two critical factors: the amount of light shone onto the sample and the temporal resolution. Conventional setups where one point in space is imaged after the other, as in confocal Laser Scanning Microscopy, are usually very slow and induce substantial photobleaching of the probes. *Selective Plane Illumination Microscopy*, also known as *Light Sheet Microscopy*, effectively reduces the volume sampling time and the excitation light dose by simultaneously exposing and imaging all the points lying on a plane.

We will show how one can build an illumination system with several simultaneous light sheets and achieve faster volumetric acquisitions. To increase the temporal resolution we will pair this particular illumination scheme with *Compressed Sensing*. This method operates by discarding some of the available information and making up for it in a post-measurement image regularization.

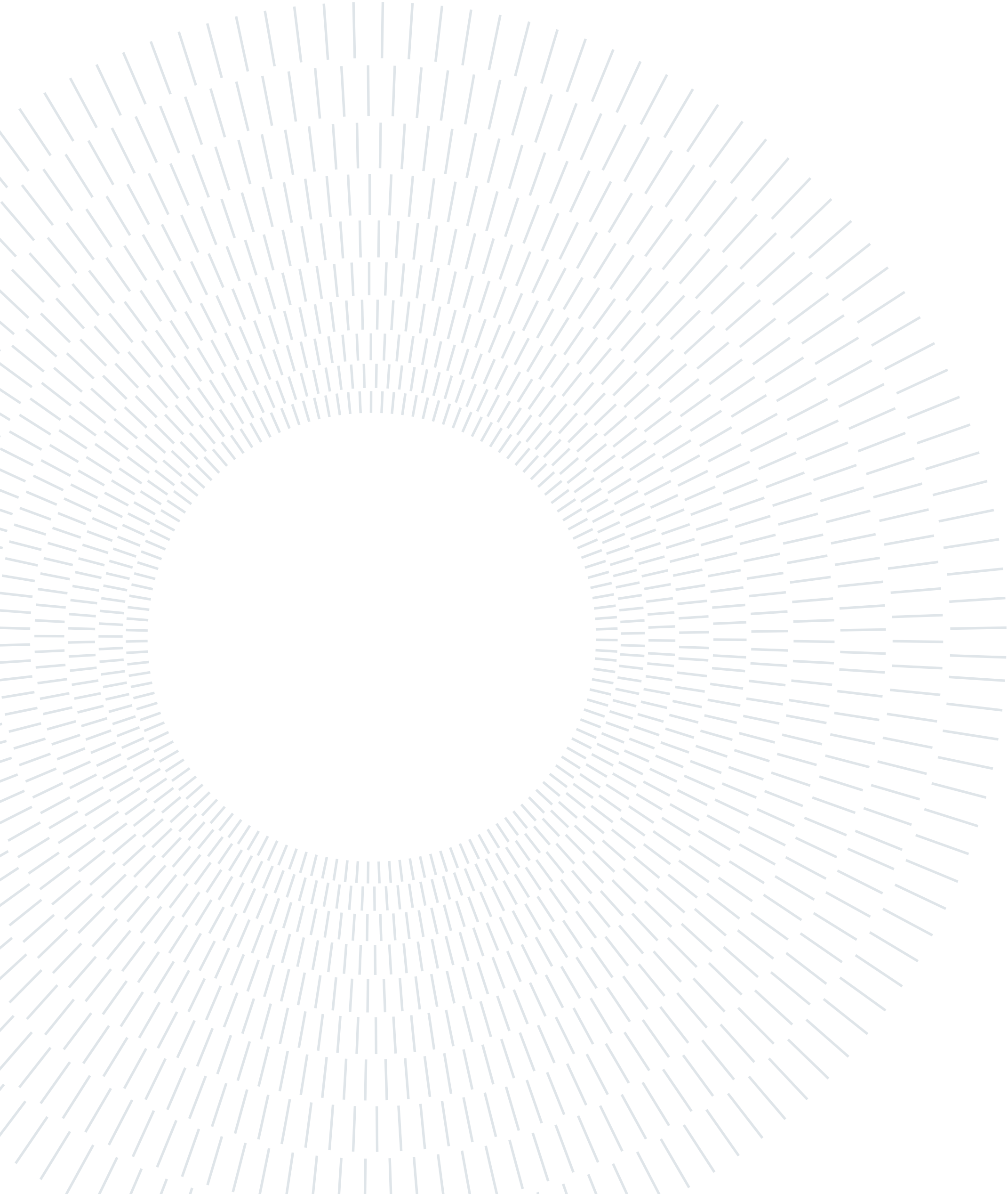

1 | Fast imaging of volumetric fluorescence

1.1. 4D fluorescence microscopy

Selective Plane Illumination Microscopy (SPIM, also known as Light Sheet Microscopy, LSM) uses a cylindrical lens to focus a Gaussian beam in one direction and create a planar sheet of light. As shown in Fig. 1.1, the light sheet is focused onto a sample to exclusively excite fluorophores lying on the plane drawn by the beam. The detection objective is then placed perpendicularly to the illumination direction, it collects the fluorescent emission and images it on a pixelated CMOS camera. When compared to conventional techniques like Epifluorescence, Confocal and Two-photon microscopy, SPIM offers a greatly increased acquisition speed, low photobleaching (see Fig. 1.2), good sample penetration and the ability to image bigger volumes [1].

The reduced photobleaching of biological samples achieved by SPIM is fundamental in most fluorescent microscopy applications, however, we want to focus our attention on the increased volume acquisition speed that can be achieved with this kind of microscope.

In conventional SPIM the sample is mounted in an low concentration gel cylinder that is moved back and forth through the light sheet to subsequently image different planes and obtain a series of volumes. This procedure limits the scanning frequency to a few volumes per second as the specimen and the gel can be damaged by the fast periodic motion [2]. Keeping the sample stationary and jointly move the light sheet and the heavy detection objective is a possible solution. Nevertheless, mechanical problems arise before one can reach sufficient speeds. Fahrbach et al. [2] solved these problems using tunable optic elements to move the detection focus plane on the scanning illumination sheet. Their microscope had no moving parts and allowed to image 17 planes at 510 frames per second, which corresponded to 30 volume scans per second.

Under the hypothesis that the biological process of interest is perfectly periodic (e.g., heart beat), it has been shown [5, 6] that is possible to use a standard SPIM setup

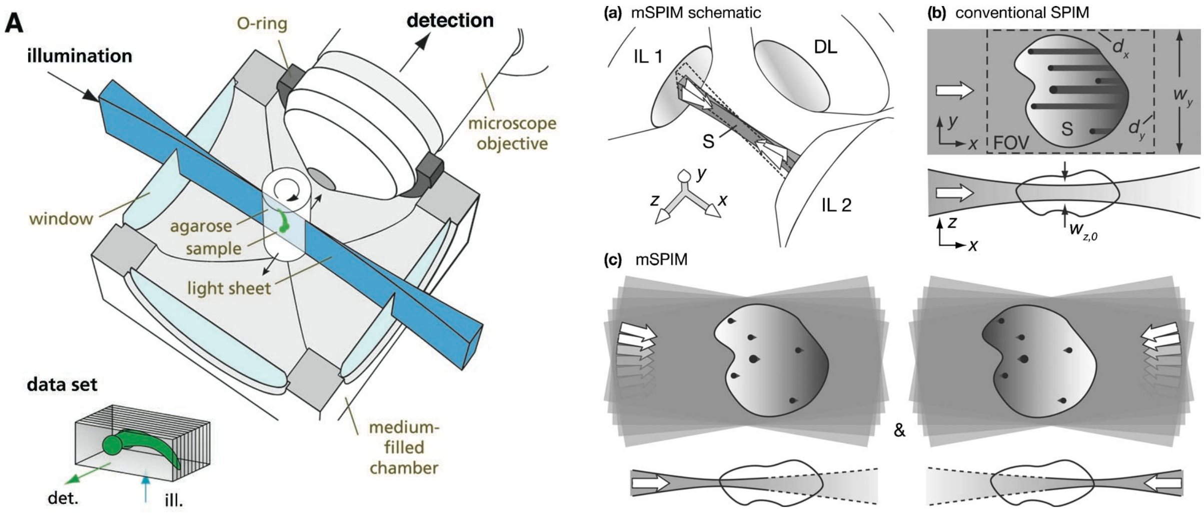

Figure 1.1: **Selective Plane Illumination Microscopy.** The left panel shows the distinctive characteristic of SPIM: the perpendicular orientation of illumination and detection. The detection objective is usually kept stationary and the sample is translated across the light sheet to image different planes. The right panel shows how Multidirectional SPIM [3] uses pivoting light sheets coming from two sides to avoid striping artifacts (shadows) and uneven illumination due to absorption and scattering. Figures taken from Huisken et al. 2004, left panel [4] and Huisken et al. 2007, right panel [3].

to subsequently acquire movies of different planes with a spacing of 1–2 µm along the detection axis. For each plane, the camera can easily follow the heart movement, covering 4 or 5 of its cycles. The resulting data set is composed of independent movies, where the periodic contractions are recorded with high temporal resolution and a random relative phase. Therefore, to produce a coherent 4D reconstruction, one needs to perform a computational synchronization of the cardiac cycles. However, Sacconi et al. [7] point out that these type of systems would not detect irregular events.

Recently, systems with increasing complexity and costs have been proposed. Among these we can find: Lattice light sheet microscopy [8], volumetrical parallelized acquisition [9, 10] and microscopes with multiple illumination planes each imaged by a dedicated camera (Sacconi et al. used seven cameras and operated at 500 fps for a 400 × 400 pixel active sensor [7]). One system that allows to reach very high scanning speeds is Swept confocally-aligned planar excitation (SCAPE) microscopy [11], where the speed limit is set by the detection camera frame rate. For example, the combination of this technique with a cooled image intensifier camera (which reached 12719 frames per second for a 640 × 148 pixel active sensor) achieved acquisition speeds beyond 100 volumes/s (making analysis of blood cells motion possible) [12].

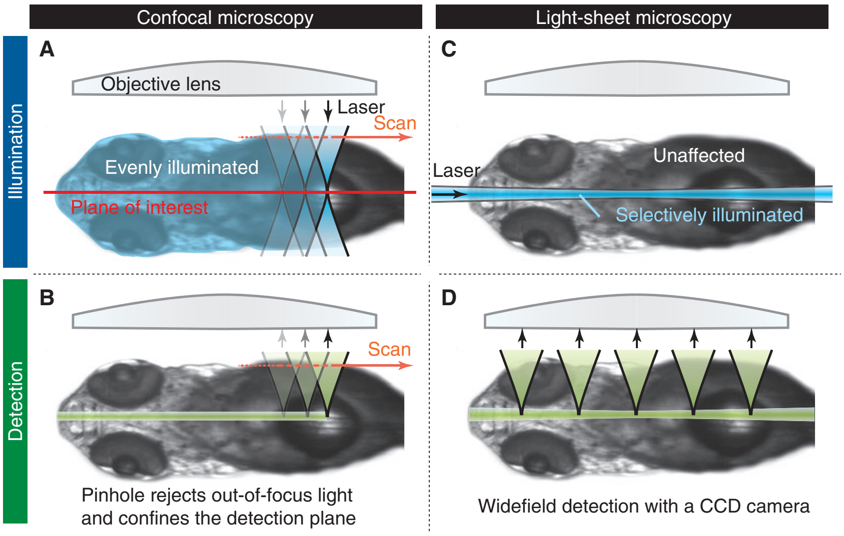

Figure 1.2: **Comparison between Confocal microscopy and Selective Plane Illumination Microscopy.** Confocal microscopy uses point illumination and point detection: a pinhole in front of the detector severely attenuates light coming from out of focus planes. The point nature of a confocal microscope results in long acquisition times as we either have to scan the beams across the sample or we have to subsequently change the pinhole location to image different points. The last method is faster and is usually implemented by spinning a disk with different pinholes. Once a plane is completely imaged, one can move to the next by translating the objective along the detection axis and create a 3D image. For example, exposing a single point for 1 µs [4] it takes at least 2.1 s to sample a matrix of dimension $256 \times 512 \times 16$. Moreover, due to fluorophores saturation at high excitation intensities, one is not allowed to speed up the acquisition by reducing the exposure time and increasing the laser power. Another drawback of this technique is that the excitation light is absorbed and scattered by all the molecules in its path, even those that are out of focus and not currently imaged (as shown in panel A). This limits the penetration depth to around 100 µm [1] and produces high photobleaching of the fluorescent markers. Figure taken from Huisken et al. [1].

1.2. Compressed sensing

When we study an unknown object, we usually perform a number of measurements that allows us to capture all the information that our instrument makes available.

With *Compressed sensing* we strive to efficiently gather information to reduce the number of measurements needed to collect the most relevant features [13]. In particular, compressed sensing allows to increase the temporal resolution of 4D scans as it can reduce the number of measurements needed to reconstruct each volume.

The basic concepts of compressed sensing are the following. An unknown vector $\boldsymbol{x}$ of dimension N can be sampled through a measurement matrix $\boldsymbol{\Phi}$ (with M rows and N columns) that translates its information into quantities $\boldsymbol{y}$ that we can easily record and analyse:

$$\boldsymbol{y} = \boldsymbol{\Phi} \cdot \boldsymbol{x}. \tag{1.1}$$

To find $\boldsymbol{y}$ we need to perform M different measurements as each value $y_m = \boldsymbol{\varphi}_m \cdot \boldsymbol{x}$ is the projection of $\boldsymbol{x}$ on $\boldsymbol{\varphi}_m$, the m-th row of $\boldsymbol{\Phi}$.

If $M = N$, the problem is said to be determined: we have one measured value y_m for each degree of freedom of $\boldsymbol{x}$. On the other hand, with compressed sensing we aim to perform a smaller number of measurements than normally necessary, that is, M becomes smaller than N. This condition leads to an ill posed problem, as it can have zero, one or multiple solutions. In this case, we can look for a *Least square* solution. The latter is defined as the the vector that minimizes the squared distance between $\boldsymbol{y}$ and $\boldsymbol{\Phi} \cdot \boldsymbol{x}$ (i.e. the loss function):

$$\underset{\boldsymbol{x}}{\operatorname{argmin}} \Big(\big\| \boldsymbol{y} - \boldsymbol{\Phi} \cdot \boldsymbol{x} \big\|_{l_2}^2 + \tau \mathcal{R}(\boldsymbol{x}) \Big). \tag{1.2}$$

In the last equation, $\tau\mathcal{R}(\boldsymbol{x})$ is a “regularization” or “penalty”function that we add to promote certain features in the solution. In this way, $\boldsymbol{x}$ will minimize both the loss function and the penalty function with a relative priority given by the parameter τ (Calisesi et al. [13] describe how the l_1 norm is the regularization function most suited for compressed sensing as it promotes sparse solutions).

The choice of the measurement matrix $\boldsymbol{\Phi}$ is crucial for a good reconstruction of compressed data: we want to create redundancy in each measurement so that we can skip some of them and still uniformly sample the whole $\boldsymbol{x}$ space. This constraint immediately makes orthogonal basis unsuitable for compressed sensing as removing a base element leaves a degree of freedom of $\boldsymbol{x}$ completely unmeasured.

To express this concept in a more formal way, we can say that if the sample $\boldsymbol{x}$ exhibits some regularity, we can look for a basis where its representation $\boldsymbol{w}$, such that $\boldsymbol{x} = \boldsymbol{\Psi} \cdot \boldsymbol{w}$, has a smaller number of non-zero coefficients. In this case, the best measurement matrix for the compressive sensing of $\boldsymbol{x}$ is one that is highly *incoherent* with $\boldsymbol{\Psi}$. That is, we ask that any two vectors of $\boldsymbol{\Phi}$ and $\boldsymbol{\Psi}$ should be uncorrelated [14].

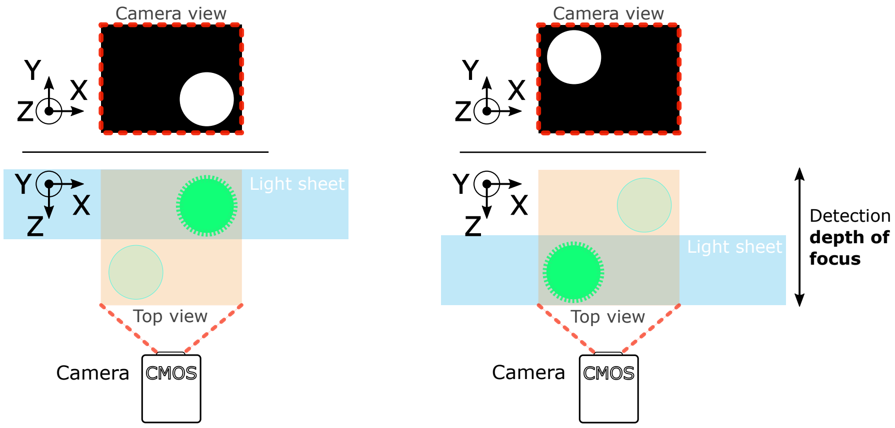

Figure 1.3: **Modified Light Sheet acquisition.** Optical sectioning along the z-axis is achieved by translating the light sheet within the detection depth of focus. In this particular example, a volume with two fluorescent beads can be reconstructed with two measurements (i.e., camera images) as the measurement matrix is the 2×2 Identity matrix.

1.3. Compressed sensing light sheet

To introduce compressive sensing in fluorescence microscopy, we needed to formalize the fluorescent emission from a given point in the sample. Fluorescence intensity is the product between the illumination intensity and the concentration of fluorophores. Let $\boldsymbol{x}_{(i,j)} \in \mathbb{R}^N$ be the unknown fluorescence distribution along the z-direction for a given (i, j) point in the XY plane. Moreover, let $\boldsymbol{\varphi}_m \in \mathbb{R}^N$ be the z-modulated illumination light pattern that we project during the acquisition of the m-th camera frame.

Each pixel of a CMOS camera integrates all the fluorescent emission generated within the Point Spread Function (PSF) of the detection objective. We worked under the hypothesis that the PSF of our system was confined in the plane parallel to the camera sensor (XY) and elongated along the axial direction (Z). In other words, we wanted a detection objective with a depth of field long enough to cover the z-dimension of our volume of interest. Fig. 1.3 shows a fluorescence microscope built with such PSF: each (i, j) pixel in the XY plane integrates the fluorescent emission along the z-direction.

Under these hypothesis, the intensity $y_{(i,j),m} \in \mathbb{R}$ recorded by the (i, j) camera pixel is given by:

$$y_{(i,j),m} = \boldsymbol{\varphi}_m \cdot \boldsymbol{x}_{(i,j)}, \tag{1.3}$$

where the scalar product formally performs the integration along the z-axis. If we perform M measurements, $m \in \{1, ..., M\}$, then the raw data set $\boldsymbol{y}$ is the result of the following matrix product:

$$\boldsymbol{y}_{(i,j)} = \boldsymbol{\Phi} \cdot \boldsymbol{x}_{(i,j)}. \tag{1.4}$$

As each one of the N z-planes can be illuminated or left dark, the entries of $\boldsymbol{\varphi}_m$ encode these two states with values 1 and 0 respectively.

During a SPIM acquisition, Z-planes at different depths are subsequently illuminated, so that $\boldsymbol{\varphi}_m$ has all entries equal to 0 except for a single 1, which represents the illuminated section. As it turns out, the SPIM measurement matrix is the Identity matrix. This means that $\boldsymbol{\Phi}_{\text{SPIM}}$ is an orthogonal basis and that SPIM is not compatible with compressed sensing. Starting from the scheme of Fig. 1.3 (implemented by Tomer et al. [15]), we need to shape the illumination in a more complex and rich way to be able to take advantage of compressive sensing. SPIM illuminates one plane at a time, while here we are going to work on the volume as a whole, moving to what is called Selective Volume Illumination Microscopy (SVIM).

Calisesi et al. [16] designed a Spatially Modulated Selective Volume Illumination Microscope (smSVIM) that uses the modified light sheet setup to implement compressed sensing for the acquisition of a single volume.

The objective of this thesis work was to build a variation of this smSVIM microscope and achieve compressive sensing of dynamic biological processes. In particular, we wanted to extend the hypothesis of sample regularity to the time dimension and reconstruct each volume taking into account information coming from neighboring time points.

2 | Selective Volume Illumination Microscopy setup

2.1. Optical Setup

Digital Micromirror Devices (DMDs) are very efficient Spatial Light Modulators (SLMs). They feature an array of micrometric mirrors that can be individually tilted to a ±12° positions (Fig. 2.1). As a result, light shining on the DMD can be deflected by each mirror along two different paths. On one of these paths we placed the sample so that by tilting each mirror we could decide whether to shine light on the sample or divert it away. In this way, the DMD applied a binary amplitude modulation mask to the illumination beam.

Due to construction requirements, the mirror rotation is performed around the diagonal axis of the squared mirror. For this reason, if we want to keep all the light beams parallel to the optical table, we need to tilt of 45° the whole DMD chip. Figure 2.1a shows how this DMD orientation allows us to work with a vertical rotation axis.

We used two telescopes to conjugate the DMD and samples planes; in this way, we could deliver to the sample the pattern created by the bright and dark pixels of the DMD (Fig. 2.2). Lenses L2 and L3 constituted the first telescope while the tube lens TL1 and the illumination objective created the second one. The DMD and the mirror M2 were both at distance f_2 from L2, with f_2 the focal distance of L2 (see Table 2.1). Moreover, the distance between M2 and L3 was f_3 and the distance between L3 and TL1 was $f_3 + f_{TL1}$. As a result of this configuration, M2 was conjugated with the back focal plane of the illumination objective; this allowed us to rigidly translate the beam in the YZ sample plane. On the other hand, to change the incident angle of the beam we could act on inclination of the DMD itself (for this purpose, it was mounted on a 3 axis rotator).

Component	Specification
CW laser	473 nm, 40 mW
MM fiber	200 µm core diameter
L1	$f_1 = 30\,\mathrm{mm}$
Cylindrical lens	$f_{CL} = 300\,\mathrm{mm}$ (y axis)
DMD	Texas Instruments DLP6500, 7.56 µm × 7.56 µm mirrors
L2	$f_2 = 150\,\mathrm{mm}$
L3	$f_3 = 75\,\mathrm{mm}$
TL1	$f_{TL1} = 180\,\mathrm{mm}$
Illumination objective	$f_{I.O.} = 40\,\mathrm{mm}$, NA $= 0.14$
Detection objective	Nikon 20×, NA $= 0.45$
Detection filter	FELH 500 nm
TL2	Nikon, $f_{TL2} = 200\,\mathrm{mm}$
Camera	Hamamatsu ORCA-Flash4.0 V2, 6.5 µm × 6.5 µm pixels, 100 fps for 2048×2048 px active sensor

Table 2.1: **Microscope optical setup specifications.** This table reports the most relevant characteristics of the optical elements of Fig. 2.2.

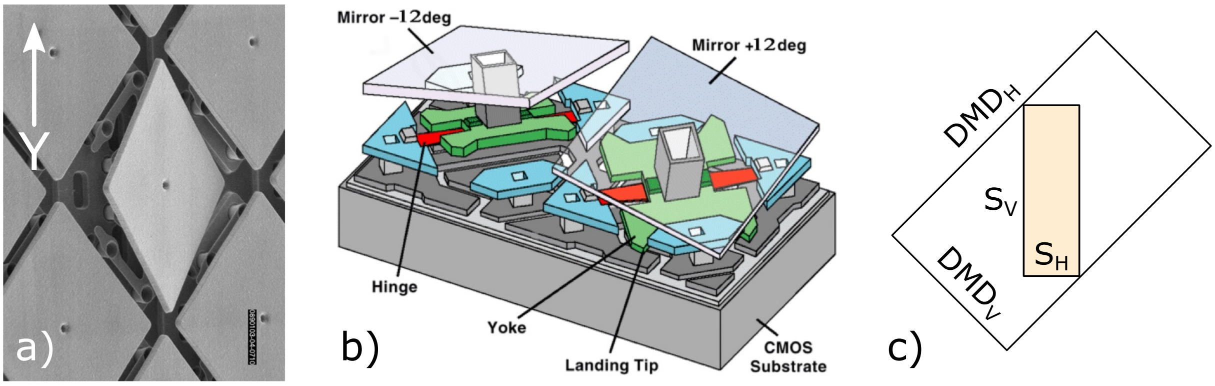

Figure 2.1: **Digital Micromirror Device. a)** Microscope image of a DMD. In particular, for our DMD (TI DLP6500) the mirror side was 7.56 µm. The shown Y direction was perpendicular to the optical table (see Fig. 2.2). Figure adapted from www.spectrum.ieee.org [17]. **b)** Electro-mechanical schematics of two DMD pixels in opposite operational states. Figure taken from Travinsky et al. [18]. **c)** The outer rectangle represents the physical DMD chip. Its dimensions are $DMD_V = 1080 \cdot 7.56\,\mu\mathrm{m} = 8.16\,\mathrm{mm}$ and $DMD_H = 1920 \cdot 7.56\,\mu\mathrm{m} = 14.5\,\mathrm{mm}$. The inner shaded area shows the biggest rectangle (with given S_V/S_H ratio) that can be drawn onto the 45° tilted DMD.

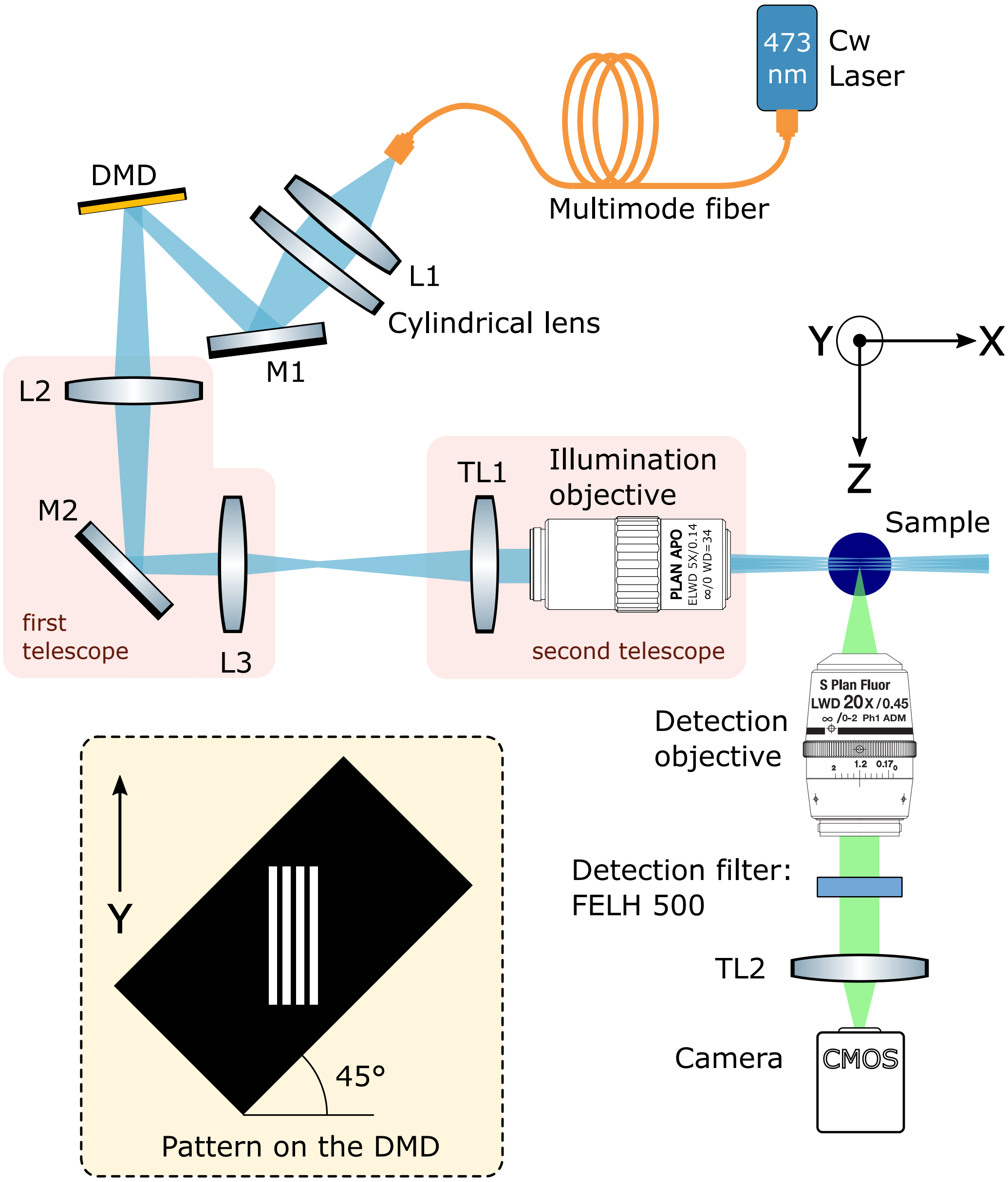

Figure 2.2: **smSVIM microscope configuration.** This scheme shows the complete setup of the microscope. The XYZ axis orientation shown in this picture will be used as reference throughout the rest of this work. The main specifications of each part are reported in Table 2.1. In the bottom left portion of this figure we see an example of how DMD patterns must be designed to create modulated illumination along the z-axis (as the four lines are parallel to the Y-axis).

Our DMD (TI DLP6500) was a matrix of 1080×1920 squared mirrors with a pitch of 7.56 µm so that the whole array had dimensions 8.16 mm × 14.5 mm. When designing this setup, we decided that the illuminated sample volume should have dimensions $s_z = 200\,\mu\text{m}$ along the z-axis and $s_y = 600\,\mu\text{m}$ along the y-axis. Therefore, the two telescopes needed to introduce a total magnification M between the DMD and sample. Using the variables defined in Fig. 2.1c, we could calculate the optimal magnification $M_{opt} = S_H/s_z$ that allowed us to use (on the 45° tilted DMD array) the largest rectangle with aspect ratio $S_V/S_H = s_y/s_z$:

$$S_H = \frac{\sqrt{2}\cdot DMD_V}{1 + s_y/s_z} = 2.87\,\text{mm}, \tag{2.1}$$

$$M_{opt} = \frac{S_H}{s_z} = 14.4. \tag{2.2}$$

Initially, we used a different L3 with $f_3' = 50\,\text{mm}$. In this case $M_{th}' = (f_2 f_{TL1})/(f_3' f_{I.O.}) = 13.5$. Even if this value was quite close to M_{opt}, this configuration proved very difficult to align. So we decided to switch to a longer $f_3 = 75\,\text{mm}$ and accepted a smaller magnification (and therefore a less efficient use of the DMD area).

With the component specifications of Table 2.1, we could expect a theoretical magnification M_{th} equal to:

$$M_{th} = \frac{f_2}{f_3}\cdot\frac{f_{TL1}}{f_{I.O.}} = 9. \tag{2.3}$$

With a calibration glass we experimentally determined that the detection magnification was 19.2 and that the illumination magnification was $M_{exp} = 8.94$.

To perform fast volumetric acquisitions, we had to use very short camera exposures. Therefore, to preserve an acceptable signal to noise ratio we needed to use high illumination intensities. With this aim in mind, we wanted to address the power loss caused by the shape difference between the circular laser beam (that arrives on the DMD after a first collimation by L1 in front of the optical fiber) and the rectangular DMD active region (see Fig. 2.1c). We introduced the cylindrical lens (Fig. 2.2) to focus the laser beam in the S_H direction and illuminate the active region in a more efficient way. The distance between the cylindrical lens and the DMD was the lens's focal length $f_{CL} = 300\,\text{mm}$.

The cylindrical lens was not able to focus the circular beam down to the limit given by its numerical aperture (circa 9 µm) because the light coming out of the multimode fiber (200 µm in diameter) had low spatial coherence. On the DMD, the partially coherent beam was focused and had a width of circa 1 mm, which was sufficient to uniformly cover the DMD active region (684 µm in the S_H direction for the experiments of chapter 4).

The long focal length of this lens partially justifies the absence of a second cylindrical lens that recollimates the beam (like in a “4f” telescope). Indeed, after testing the system with a proper cylindrical telescope, we found out that a single lens with a long focal length worked just as well. After the DMD, the divergence of the beam due to this single lens did not produce notable artifacts.

The samples were first enclosed in agarose and then lowered in a quartz cuvette filled with distilled water. This method provided index matching and prevented unwanted refractions. The cuvette had a square basis and its orientation was such that its faces were perpendicular to the illumination and detection paths. The glass of the cuvette was 1.30 mm thick and the water was confined in a square of $(10.00\,\mathrm{mm})^2$.

2.2. Light source coherence

Typical Light Sheet microscopes use coherent laser light to illuminate the sample. Indeed, laser sources are well suited for real time imaging because of their high radiance (i.e., energy density): even with short exposure times, they can provide sufficient fluorophore excitation and acceptable signal to noise ratios. However, as the right hand panel of Fig. 1.1 already points out, laser light creates striping artifacts and speckle patterns. Striping artifacts (i.e., shadows) are created by dense media within the sample as the highly directional laser light fails to recover after an obstacle [19]. On the other hand, speckle patterns come from the interference of coherent light that was scattered by different points of a non homogeneous medium.

While Huisken et al. [3] tackled these problems by using multi-directional illumination, Calisesi et al. [16] opted for an incoherent light source (an LED). Alternatively, we could actively break the coherence of the laser light by using a rotating diffuser disk that randomizes the beam wavefront [19]. The diffuser has to be kept in motion to create a uniform illumination: in this way, the speckle generated by different regions of the disk, remains on the sample for a small fraction of the exposure time and is averaged out.

To take advantage of the high intensity of a laser source while avoiding the artifacts entailed by coherent illumination, we chose to use a continuous wave diode laser coupled to a multimode optical fibre. The large core of this fibre (200 µm) allowed to achieve very good coupling efficiency and, more importantly, it greatly deteriorated the laser light coherence. The fluorescent emission of a coumarin solution exposed to a sinusoidally modulated excitation is shown in Figures 2.3 and 2.4. We rotated of 90° the DMD pattern so that the modulation was along the Y-axis and it could be directly seen by the camera.

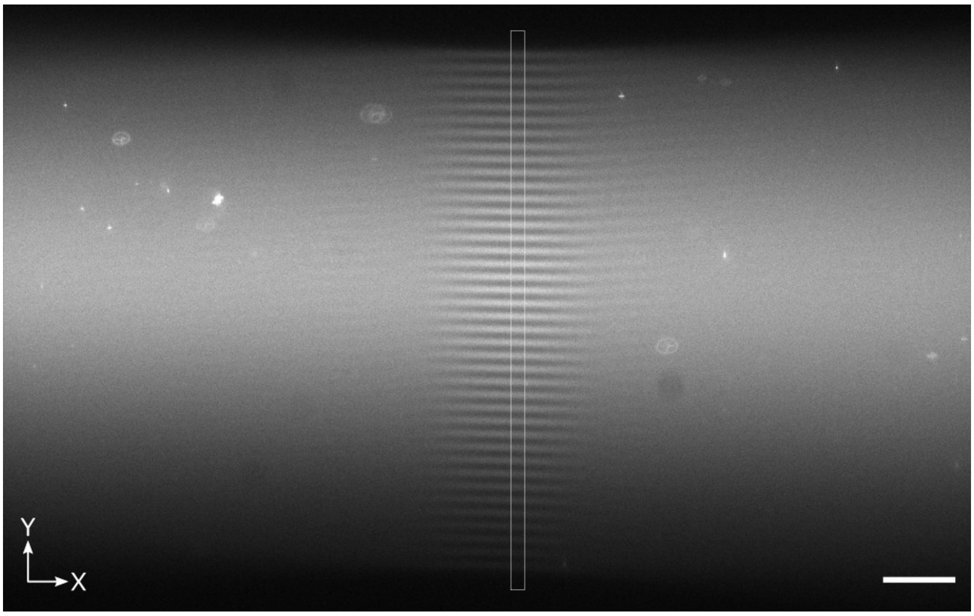

Figure 2.3: **Incoherent sinusoidal pattern.** Green fluorescent emission of a coumarin solution excited with light modulated along the Y-axis (contrary to the usual Z-axis modulation used for optical sectioning). The persistence length (along X) of the modulated region decreased as one lowered the DMD square wave period. Mertz [20] formally described the projection of an incoherent source modulated by a sinusoidal amplitude grating. The Y intensity profile of the region described by the white rectangle (averaged along X) is shown in Fig. 2.4. This frame was acquired with a 10× detection objective (instead of the 20× we used to image the zebrafish heart) to have a bigger XY field of view. Its area was $(2048 \times 0.65\,\mu\text{m})^2 = (1.33\,\text{mm})^2$. Note that we cropped this figure in the Y direction. The scale bar is 100 µm.

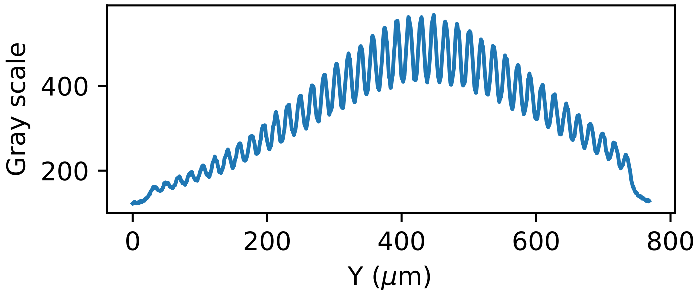

Figure 2.4: **Incoherent sinusoidal patter profile.** Intensity Y profile of the region highlighted by the white rectangle in Fig. 2.3 (we average along the X direction). The average inter-peak distance is 17.96 µm. At the borders of the profile we can notice the edges of the illumination beam.

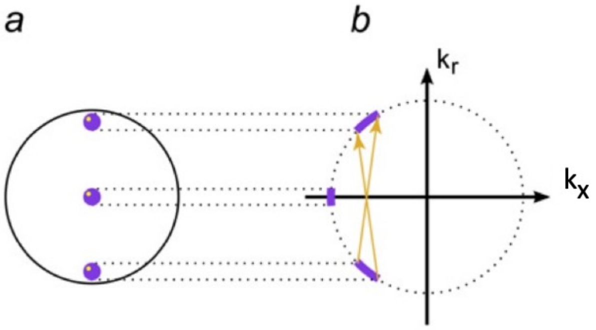

Figure 2.5: **Three beams at the back focal plane of the illumination objective. a)** The purple dots show the position of the three illumination beams. **b)** Spatial frequency components of the monochromatic light amplitude. Due to the cylindrical symmetry of the objective, the radial wave vector k_r can represent modulation along the Z or Y axis. Figure adapted from Gustafsson et al. [21].

2.3. Excursus on coherent sinusoidal patterns

Using coherent light it is possible to create sinusoidal patterns through interference. The simplicity of sinusoidal patterns allows to produce high contrast modulation in a quite straightforward way. After replacing the multimode fiber with a single mode one, we created on the DMD a square wave pattern of period T oscillating between 0 and 1 (like in the example of Fig. 2.2). We chose to modulate the pattern along the Y direction to be able to visualize the results using the camera and a fluorescent coumarin solution as sample. In the back focal plane of the Illumination objective we could access the Fourier transform of the this pattern: the spectrum of our square wave featured points along the Y-axis positioned at odd multiples of the fundamental spatial frequency (given by $1/T$). Since the DMD pattern had a non-zero average over one period (it oscillates between 0 and 1), we also had a continuous component beam that lied at the origin of the Fourier plane.

Among the beams generated by the square wave, we worked on three of them: the continuous component and the two symmetric points corresponding to $\pm 1/T$ (Fig. 2.5a). Suppressing the central point and letting the other two interfere we were able to generate a perfectly sinusoidal pattern (Fig. 2.6). We can notice that the Y modulation remains visible across the entire X range (with straight lines that only show a slight and periodic loss of contrast). This indicates that the persistence length of patterns generated through interference is much longer than the persistence length of incoherent patterns. This procedure was thoroughly described in Mertz [20], with the difference that they used a phase mask to create the sinusoidal wave (while a DMD works as an amplitude mask).

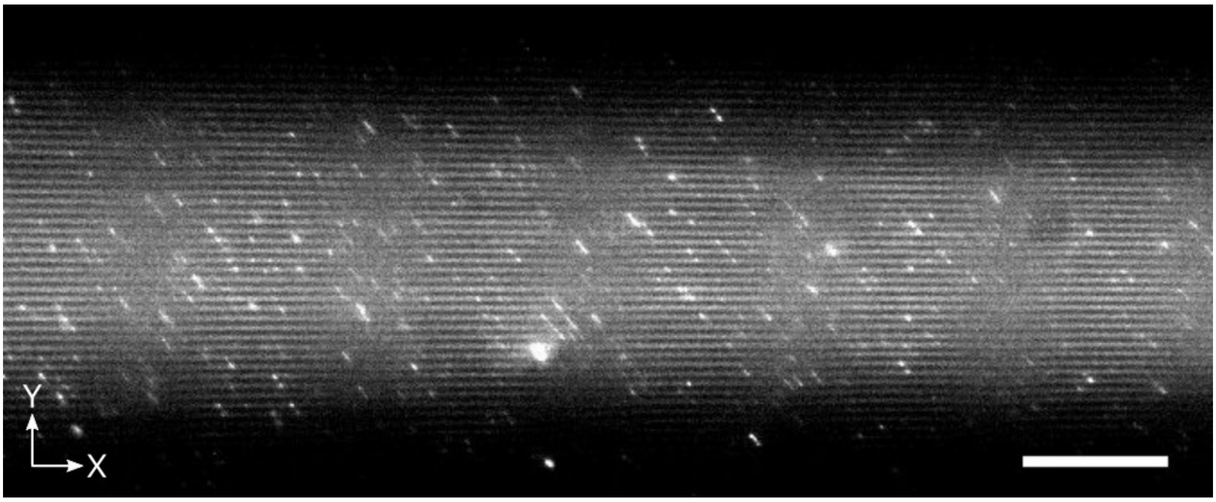

Figure 2.6: **Coherent sinusoidal patter with suppression of the central beam.** Green fluorescent emission of from coumarin solution excited with blue light modulated along the Y-axis (contrary to the usual Z-axis modulation used for optical sectioning). This frame was acquired with a 10× detection objective and the scale bar is 100 µm.

We rudimentarily performed the suppression of the central beam by using the tip of a piece of paper, and when this operation did not work properly we could simultaneously see the patterns generated by the interference of two or three beams: Fig. 2.7 shows how the partial elimination of the central beam produced different modulations in different regions. In particular, we can see that in the lower portion of the illumination the central beam was still present and made the modulation period twice as long (see also the profile of Fig. 2.8).

The interference of three beams was exploited in Gustafsson et al. [21]. In Fig. 2.5b we can see how the k_x domain has two separate regions: one created by the central beam and one created by the two beams with non-zero radial frequency. Heuristically, we can expect that the interference of light with different k_x components will generate a pattern with modulation along the X direction. Figure 2.9 shows the interference of the three illumination beams. We can notice that there are two vertical regions which did not exhibit any Y modulation. Moreover, the sine curves left and right of this region had a phase difference of π (Fig. 2.10). If we decreased the period of the DMD square wave, the illumination modulation in the X direction became more frequent, with the areas that mark a phase shift becoming closer to one another.

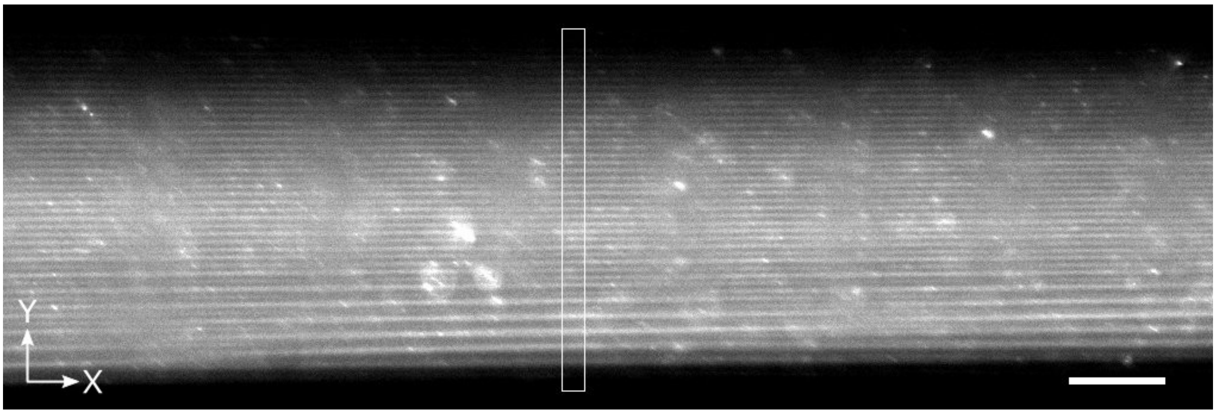

Figure 2.7: **Coherent sinusoidal patter with partial suppression of the central beam.** The Y intensity profile of the region described by the white rectangle (averaged along X) is shown in Fig. 2.8. This frame was acquired with a 10× detection objective and the scale bar is 100 µm.

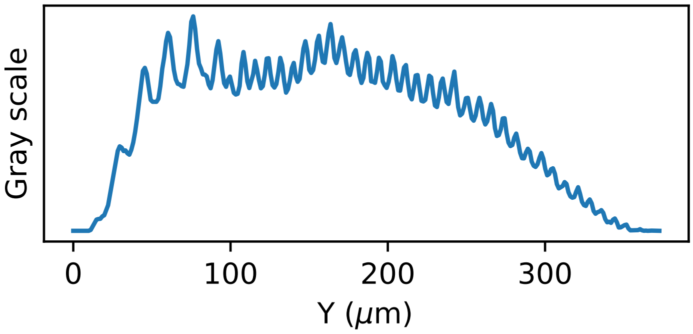

Figure 2.8: **Illumination profile resulting with partial suppression of the central beam.** Intensity profile of Fig. 2.7. We can see how the modulation period was doubled before $Y = 100\,\mu\text{m}$.

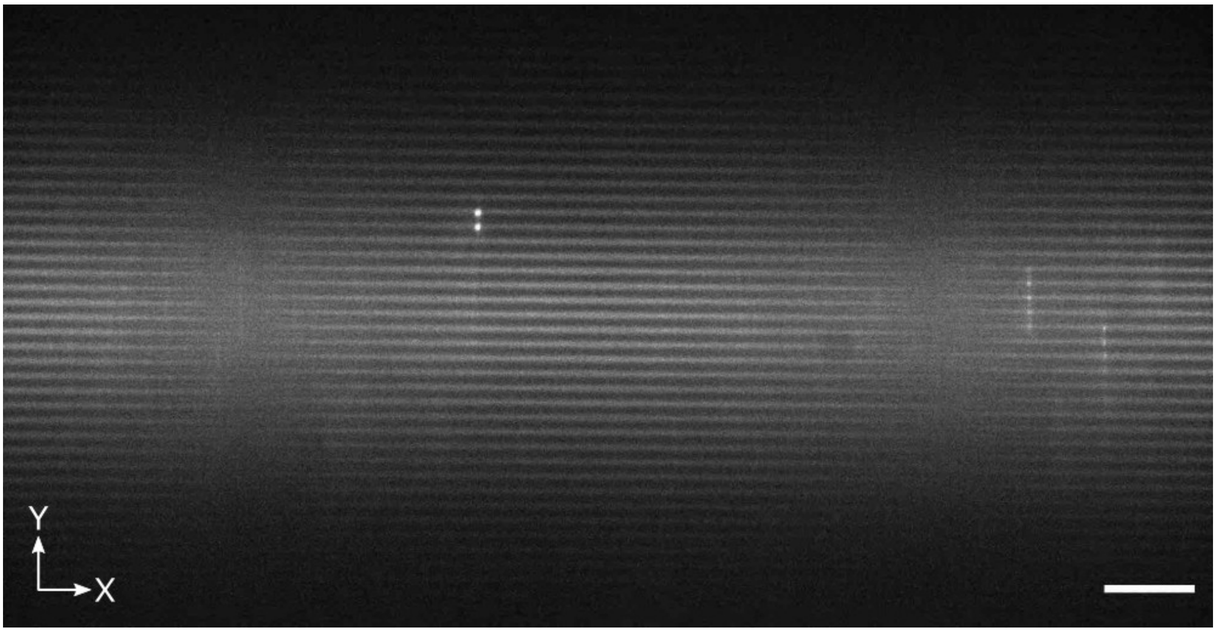

Figure 2.9: **Three beam interference pattern.** We can recognize a marked modulation along the X axis and notice how sinusoidal profile in different regions are shifted relative to one another (see the two profiles in Fig. 2.10). This frame was acquired with a 10× detection objective and the scale bar is 100 µm.

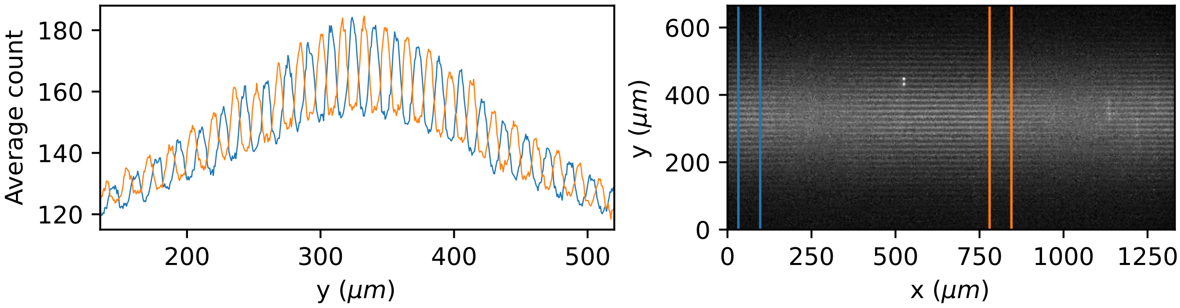

Figure 2.10: **Phase shift in a three beam interference pattern.** Y-profiles, averaged in the X direction, of the interference pattern of Fig. 2.9. Two different portions of the X axis have sinusoidal modulation with a relative phase shift of π.

2.4. DMD blazed grating effect

DMDs are relatively inexpensive Spatial Light Modulators (SLMs) that offer high operational speed: compared to Liquid Crystals on Silicon SLMs they have a lower cost of a factor 2-10 and an imaging rate higher of a factor 5-10 [22]. However, their pixel structure can give rise to implementation problems. In particular, when paired with coherent or semi-coherent light sources they generate interference effects due to their periodic structure. The 2D array of tilted micromirrors acta as a diffraction grating: each square mirror produces a single slit envelope (a 2D $(\mathrm{sinc})^2$) that modulates the intensity of the diffraction orders (generated by the interference of light coming from different mirrors) [23].

The position of the envelope peak depends only on the incident light angle and on the tilt angle of the mirrors (as it comes from single slit diffraction). If we define all angles with respect to the normal of the DMD plane, the incident angle θ_i, the mirror tilt angle θ_{tilt}, and the envelope peak reflection angle $\theta_{r,env}$ satisfy the following expression: $|\theta_{r,env}| = |\theta_i + 2\theta_{tilt}|$. On the other hand, the positions of the zeros of the $(\mathrm{sinc})^2$ envelope also depend on the mirror dimensions and on the wavelength of the incident light.

The position of the 0^{th} order depends exclusively on the incident angle with $|\theta_{r,0}| = |\theta_i|$. All other diffraction orders are also influenced by the grating pitch and the illumination wavelength.

When one diffraction order overlaps with the envelope peak, the order is said to be “blazed”. Blazing conditions are used to efficiently shine light on the sample as the envelope concentrates most of the incident power in a single order. To reach a blazing configuration, we can change the incident angle to move non-zero orders relative to the envelope peak.

The situation becomes more difficult when working with multiple illumination wavelengths that simultaneously need to be in a blazing condition. Three-colour Structured illumination microscopy (SIM) was achieved using a complex opto-mechanical setup: a controlled mirror slightly adjusted the path for two alternating wavelength and a separate optical path carried a third wavelength [22]. Alternatively, one can control the output wavelength of a diode laser (by varying its temperature) to fine tune the ratio between the two illumination wavelengths and perfectly work at a blazing configuration [24, 25].

The blazed grating effect turned out to be negligible in our setup as we used laser light that exhibits low spatial coherence after travelling in a multimode fiber. If we had coupled the laser to a single mode fibre the effect would have been of primary importance during the system alignment.

2.5. Increasing the detection depth of focus

As we already anticipated in the first chapter (section 1.3), to use a SVIM microscope we need a sufficiently large detection depth of focus to uniformly integrate the emitted fluorescence along the Z direction.

Tomer et al. [15] devised a SPherical-aberration-assisted Extended Depth-of-field light sheet microscope (SPED-LS) where sample and detection objective were kept stationary while the light sheet was scanned within the detection depth of focus (just like in Fig. 1.3). The depth of focus was purposefully extended in the axial direction (i.e., Z-axis) by introducing spherical aberrations in the detection path. For this purpose, a layer of medium with refractive index higher than air (for objectives that are aberration corrected in air) was inserted between the sample and the detection objective. The PSF axial FWHM increased with the layer's refractive index and thickness.

We found that the depth of focus of our setup was sufficiently large to uniformly image our volume of interest (with a Z extent of 76.5 µm). The elongation of the PSF was caused by intrinsic aberrations in the detection arm: we used a detection objective designed to work in air (20× Nikon, NA = 0.45) to image a sample that was placed behind layers of glass and water. Over the nominal air working distance of the objective (8.2 mm) we find circa 4 mm of water and a 1.30 mm slab of glass.

We compared the PSF of our system with the PSF of a water immersion objective: a 20× Olympus with NA = 0.50 (which paired with the Nikon tube lens provided a 22.3× magnification). This objective was placed directly inside the cuvette and was designed to have no aberrations when detecting light emitted inside water. Immersion objective are widely used in conventional SPIM setups that translate the sample across the detection focus plane.

For the comparison we used green fluorescent beads with a diameter of 160 nm suspended in an agarose gel. Since their dimension was below the diffraction limit, they behaved like point sources and we could directly observe the detection PSF. Figures 2.11 and 2.12 show the reconstruction along Z of a volume filled with beads: we used the DMD to subsequently illuminate 16 planes of thickness 4.78 µm. This thickness corresponded to 4 DMD pixel diagonals and was limited by the illumination objective numerical aperture. The reconstructed volume had a Z axis extent of 76.5 µm, a range that we later used for the zebrafish heart.

As shown in Fig. 2.11 with our setup (air objective) we uniformly found beads at different Z planes. On the contrary, as shown in Fig. 2.12, with the water objective we could only

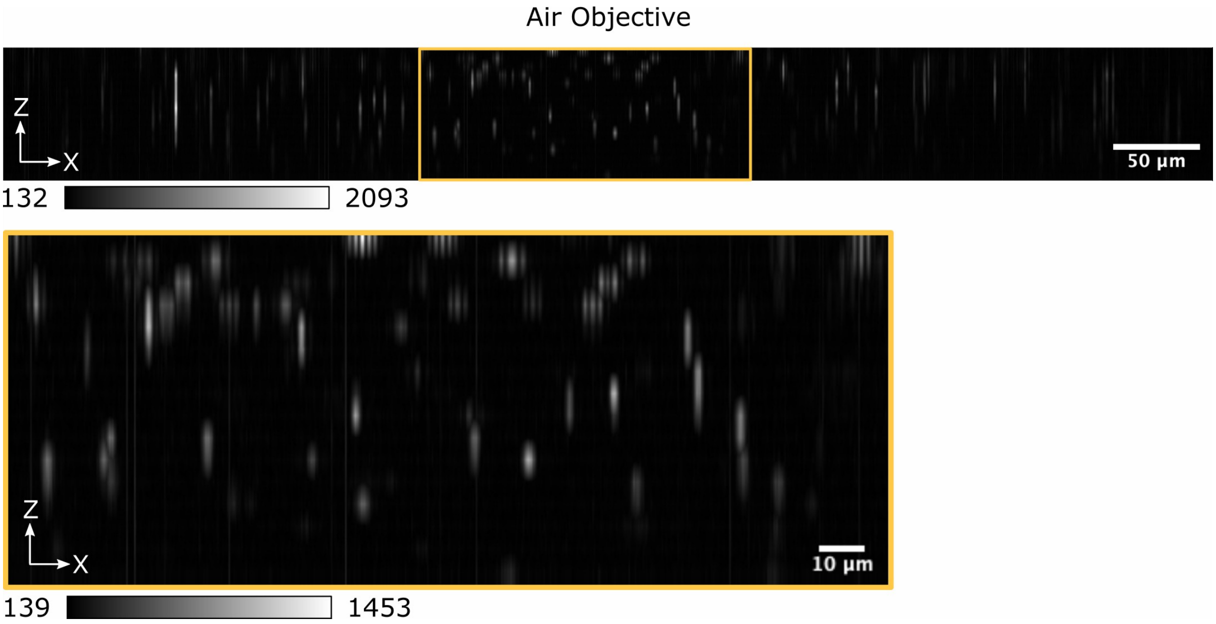

Figure 2.11: **Air objective: beads sectioned by Z-scanning light sheet.** The ROI enclosed in the yellow rectangle (190 µm and 76.5 µm long in the X and Z directions respectively) is magnified in the lower portion of the figure. This region is centered around the X point of focus of the illumination objective.

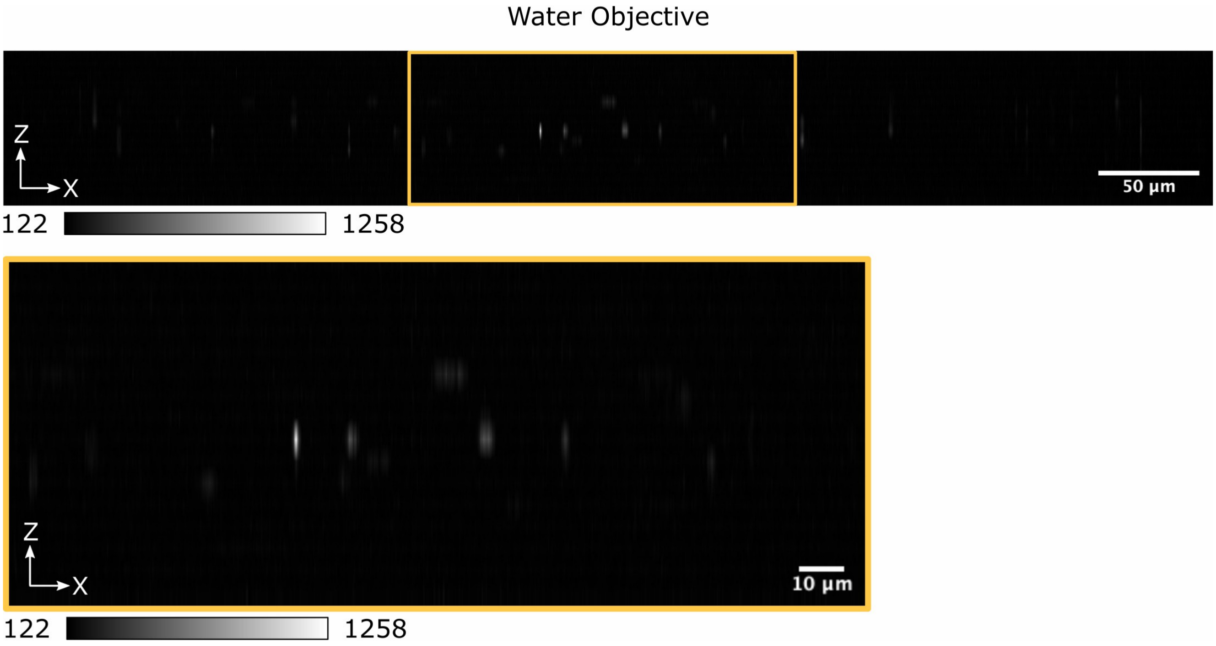

Figure 2.12: **Water objective: beads sectioned by Z-scanning light sheet.** The ROI enclosed in the yellow rectangle (190 µm and 76.5 µm long in the X and Z directions respectively) is magnified in the lower portion of the figure. Beads are detected only in a very small region around the focus plane, positioned in the middle of the ROI Z range.

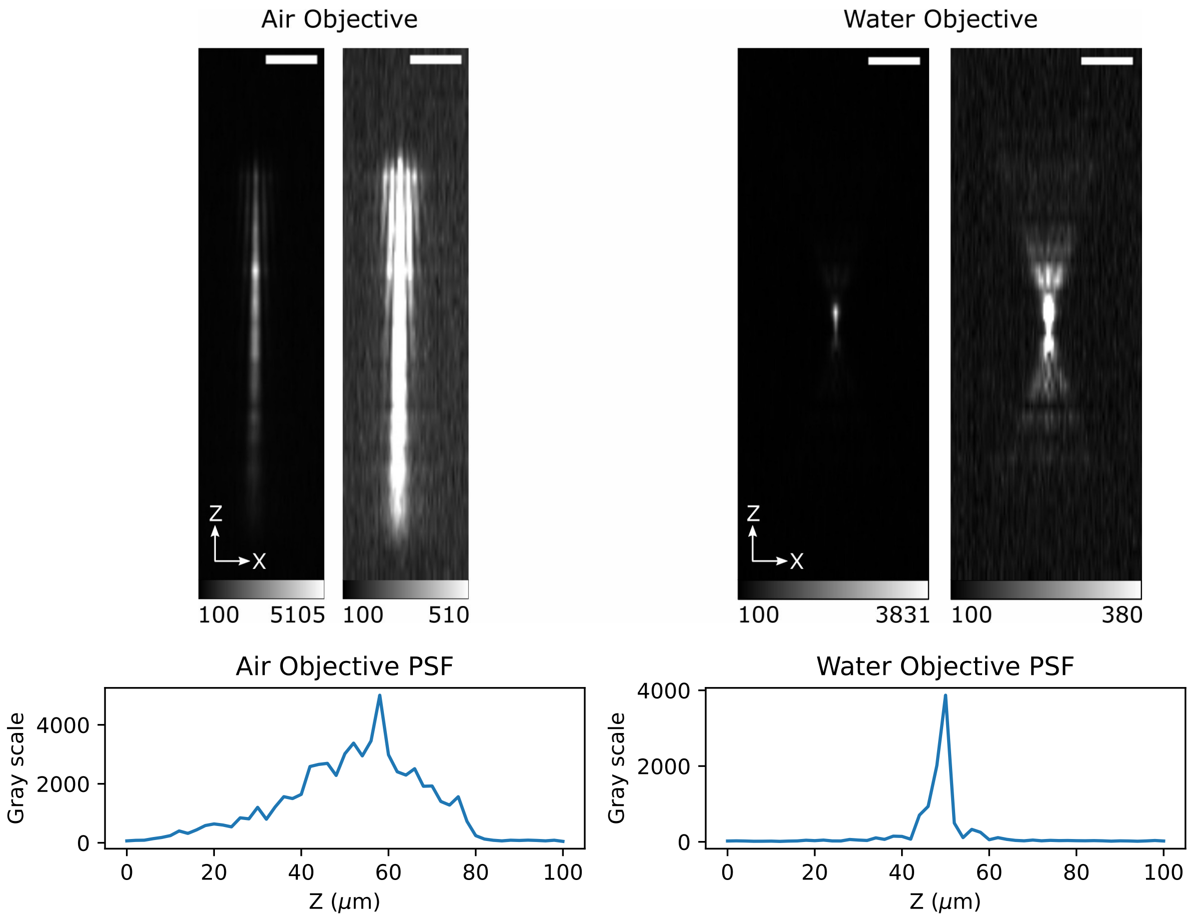

Figure 2.13: **Comparison between measured PSF.** The two PSFs were measured by translating sub-diffraction limit beads (160 nm in diameter) in a thick light sheet (76.5 µm in the Z direction) parallel to the XY plane. The beads are translated along Z by steps of 2 µm for a total of 50 steps. The top panels show (with two different contrasts) the XZ planes that contain the PSF brightest point. The two graphs report the PSF Z-profiles in the XY coordinate of its brightest point. The scale bars are 10 µm long.

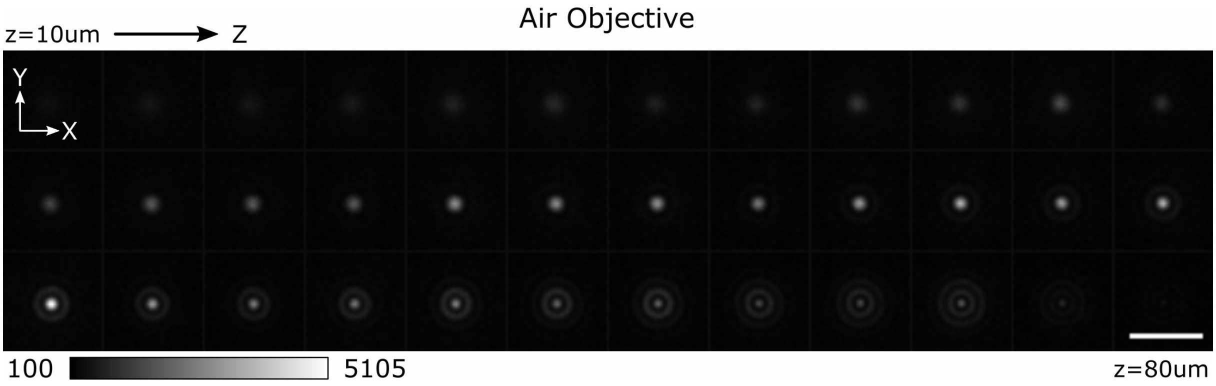

Figure 2.14: **Air objective PSF: sections at different depths.** We show 36 of the 51 frames acquired: The Z separation between each frame (from left to right and top to bottom) is 2 µm. The scale bar for the XY planes is 10 µm long.

see few beads in a small region around the detection focus plane. These tests showed us that depth of field of the aberration corrected immersion objective was insufficient for our purposes. Fig. 2.11 highlights an asymmetry in the detection PSF: along the Z direction, beads went from a simple bell shape to a more complex structure with disks. On the other hand, beads at the X borders were elongated along Z because of the limited depth of focus of the illumination objective. At the borders of the field of view the light sheet was out of focus, so it did not provide optical sectioning and it illuminated a single bead for more than one frame.

Finally, we directly measured the detection PSF. To do so, we illuminated the whole volume of interest (76.5 µm in Z) and we used a micrometric translator to move the sample by steps of 2 µm along the Z-direction. We recorded 51 frames to cover a span of 100 µm in the Z direction. In this way, we could follow a single bead as it passed through different portions of the detection PSF. Fig. 2.13 shows XZ planes of the measured PSF of the two objectives.

As we can see the aberrated air detection offered an elongated PSF that more or less spanned across the z region of interest (ROI). Figure 2.14 further highlights how the PSF was asymmetric along the Z axis and exhibited rings only on one side. Using this information, we could potentially apply a deconvolution algorithm [15] to clean the reconstruction of Fig. 2.11.

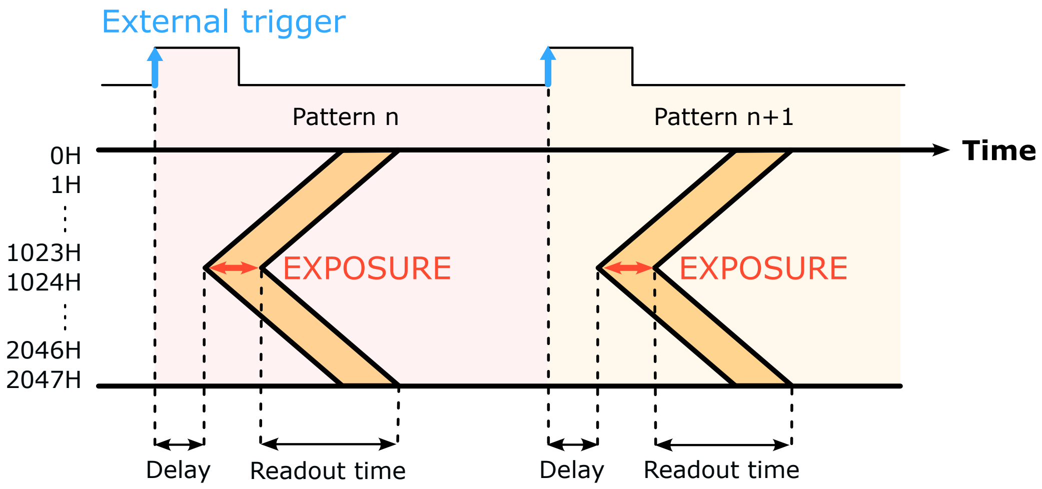

Figure 2.15: **Camera acquisitions with external edge trigger mode.** The dark orange areas show when different sensor lines (numbered on the left) are exposed.

2.6. Camera synchronisation and acquisition rate

We used an Hamamatsu ORCA-Flash4.0 V2 with a 2048 × 2048 pixel sensor. Its user manual [26] tells us that the sensor read out is performed by using a rolling shutter: it starts by reading the central horizontal lines (1023H and 1024H) and then it simultaneously moves up (until line 0H) and down (until line 2047H) to read all pixels. The camera takes $\tau = 9.744\,36\,\mu\text{s}$ to read a single line. Therefore, if we have V_n horizontal active lines (symmetrically distributed around the middle of the sensor) the total read out time is equal to $V_n/2 * \tau$. In the manual we also find that the exposure time can range from 1.004 ms to 10 s.

Our acquisition scheme required one camera frame for each DMD pattern. To synchronise the two devices we used the trigger signal emitted by the DMD: at the beginning of each patter, a rising edge was sent to the camera. The distance between two trigger impulses was given by the DMD pattern exposure time, a parameter that we could precisely set at the beginning of a measurement. We used the camera in its “Edge trigger mode”, whose time scheme is shown in Fig. 2.15. The maximum frame rate achievable in this operation mode is given by the following expression:

$$fps_{max} = \frac{1}{V_n/2 \cdot \tau + Exposure + Delay}, \tag{2.4}$$

where the $Delay = 9 \cdot \tau = 87.7\,\mu\text{s}$ is a constant time between the trigger rising edge and the exposure onset.

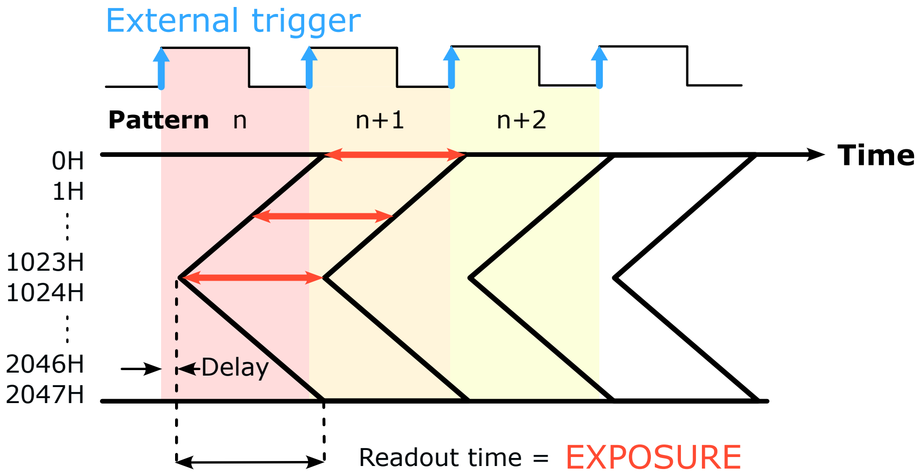

Figure 2.16: **Camera external trigger mode with synchronous readout.** The highest possible frame rate is achieved by a continuous readout of pixel lines, this condition makes the exposure time equal to the readout time. In this mode, $Delay = 18 \cdot \tau = 165.58\,\mu s$.

Once we have set the lowest exposure time possible (1.004 ms), we can increase the frame rate only by reducing the dimension of the active sensor. Since the zebrafish heart has a bigger extent in Y than it has in X, we rotated the camera by 90°. In this way, by lowering V_n we only narrow the field of view in the X-dimension. Using $V_n = 256$ (that is, 256 pixels in the Y-direction) and a pixel exposure of 1.208 ms, we could experimentally achieve an external trigger frequency of 386.3 Hz (in theory, with this parameters we could reach 393.2 Hz but, at this rate, the camera looses trigger edges too frequently).

There is another frame acquisition mode, called "Synchronous readout trigger mode", that in theory allows to reach higher frame rates. As shown in Fig. 2.16, the frame rate can be cut down to $fps_{max} = 2/(V_n \cdot \tau)$. However, we can not use this mode because different lines of a given frame are exposed to different DMD patterns. The three red arrows of Fig. 2.16 highlight this problem. They represent the exposure time of three different lines and they see different patterns: the bottom arrow mostly covers pattern n, the central arrow spans over pattern n and $n+1$ and the top arrow covers pattern $n+1$. Figure 2.17 shows the outcome of this effect: we projected a first pattern that uniformly illuminated the field of view and a second one that illuminated just its lower half.

We strove to efficiently upload patterns on the DMD. We created patterns at the beginning of each measurement to avoid using a static pre-made collection (which could not be modified between experiments). We used the DMD "pattern on the fly" mode [27] to load up to 400 patterns into the device's flash drive. After the upload, we could handpick the

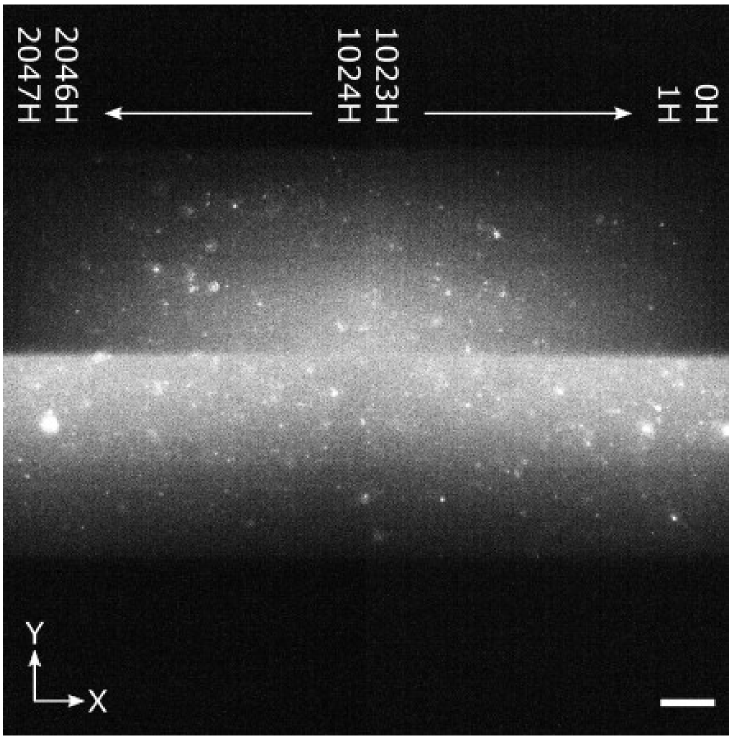

Figure 2.17: **Camera external trigger mode with synchronous readout: two patterns.** We set the DMD to project a first pattern with continuous illumination along Y and a second one where the illumination was confined in the bottom part. At the center of the frame we recognize the first pattern while in the left and right borders we see the second pattern. The camera was rotated of 90° so that V_n varies the X-width of the FOV. In this example, the active sensor was 2048×2048 pixel and it recorded the fluorescent emission of a coumarin solution through a 10× detection objective; the scale bar is 100 µm long.

patterns to be shown in the display sequence. We based our code for the control of the DMD on the code developed by Prof. Paolo Pozzi (see `https://github.com/csi-dcsc/Pycrafter6500`).

The whole microscope is managed through *ScopeFoundry*, a Python based instrument control application that manages both data acquisition and visualization [28]. ScopeFoundry allows us to interact with the hardware and to execute custom designed measurements. The code used to communicate with the different hardware components and to orchestrates the measurements can be found in the following GitHub repository: `https://github.com/marccv/smSVIM`.

3 | Volume reconstruction

3.1. Direct problem and Inverse problem

The acquisition of raw data represented our direct problem. For each camera pixel (i,j), $\boldsymbol{y}_{(i,j)} \in \mathbb{R}^M$ is the result of M measurements:

$$\boldsymbol{y}_{(i,j)} = \boldsymbol{\Phi} \cdot \boldsymbol{x}_{(i,j)}. \tag{3.1}$$

In the previous equation, $\boldsymbol{\Phi}$ is the measurement matrix and $\boldsymbol{x}_{(i,j)} \in \mathbb{R}^N$ is the unknown Z fluorescence distribution in front of the camera pixel. To reconstruct $\boldsymbol{x}$, we need to perform an inversion of the raw data produced by the direct problem. In particular, we look for a least square solution:

$$\underset{\boldsymbol{x}}{\operatorname{argmin}}\Big(\big\|\boldsymbol{y} - \boldsymbol{\Phi} \cdot \boldsymbol{x}\big\|_{l_2}^2 + \tau\mathcal{R}(\boldsymbol{x})\Big), \tag{3.2}$$

where $\tau\mathcal{R}(\boldsymbol{x})$ is a generic regularization term.

3.2. Measurement matrix

Measurement matrices built with *Hadamard* patterns have been found to work well with compressed sensing [13]. A Hadamard matrix $\boldsymbol{H}_N$, is a $N \times N$ matrix with entries $+1$ and -1 that satisfies $\boldsymbol{H}_N\boldsymbol{H}_N^T = \boldsymbol{H}_N^T\boldsymbol{H}_N = N\boldsymbol{I_N}$, where $\boldsymbol{I_N}$ is the N dimensional identity matrix [29]. We can recursively build Hadamard matrices by defining $H_1 = 1$ and, for $k \in \mathbb{N}^+$,

$$H_{2^k} = \begin{bmatrix} H_{2^{k-1}} & H_{2^{k-1}} \\ H_{2^{k-1}} & -H_{2^{k-1}} \end{bmatrix}. \tag{3.3}$$

In Fig. 3.1 we show H_{16} and its *Walsh* version with rows ordered by increasing spatial frequency. While the first row of these symmetric matrices has all values set to 1, the remaining rows have half of the entries equal to 1's and half equal to -1's (fill factor $1/2$). This property survives even if we *scramble* H_N by randomly permuting its rows and

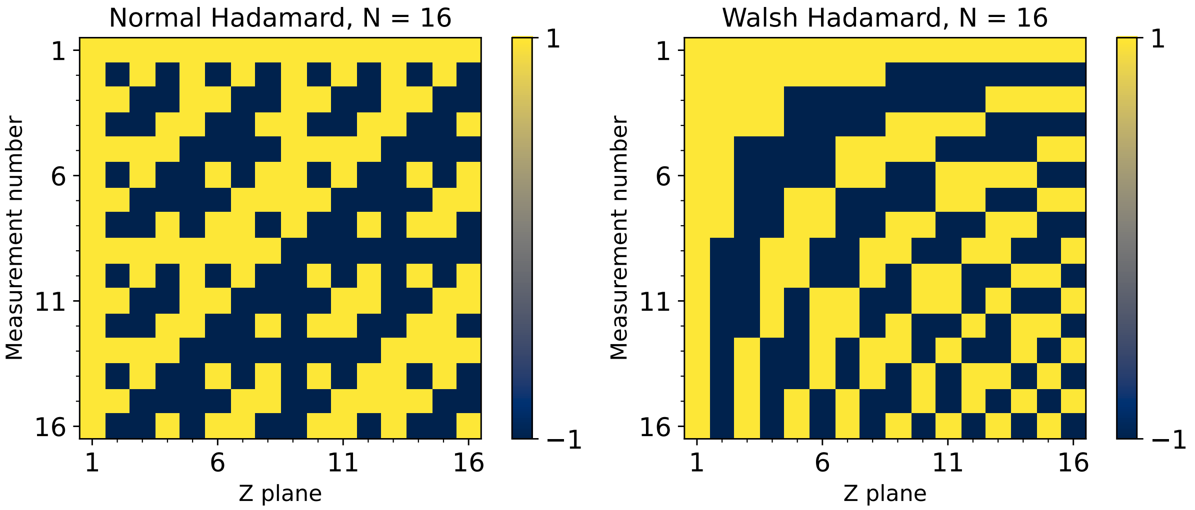

Figure 3.1: **Hadamard patterns.**

columns (Fig. 3.2).

Hadamard pattern are well suited for DMDs as they have binary entries. However, DMDs can only show 0's and 1's. This leaves us two choices: we can either replace all the -1 entries with a 0 and work with a positive measurement matrix $\boldsymbol{\Phi}$, or express each row of $\boldsymbol{H}$ (that is, each measurement) as the subtraction of two positive patterns. We called the first method *Single Frame* and the second one *Double Frame*. Here is an example of the second method applied to the m-th row $\boldsymbol{\varphi}_m = [1, -1]$ of a measurement matrix with $N = 2$:

$$y_m = y_m^+ - y_m^- = [1, 0] \cdot \boldsymbol{x} - [0, 1] \cdot \boldsymbol{x} = [1, -1] \cdot \boldsymbol{x} = \boldsymbol{\varphi}_m \cdot \boldsymbol{x}, \tag{3.4}$$

where y_m^+ and y_m^- are the physical values that we record in two subsequent camera frames.

The significant advantage of a *Double Frame* acquisition lies in its intrinsic and robust background subtraction. Moreover, the subtraction of two frames leads to a signal to noise ratio $\sqrt{2}$ times higher. The great cost we need to pay for this features, is the doubling of the number of frames needed to reconstruct a single volume.

We also explored the possibility to use a cosine basis to perform a discrete cosine transform (DCT) of the fluorescence distribution along Z. However, DCT requires patterns that are equally spaced in the frequency domain. This basis is impossible to build on the DMD as periodic patterns have periods equal to integer multiples of the pixel dimension.

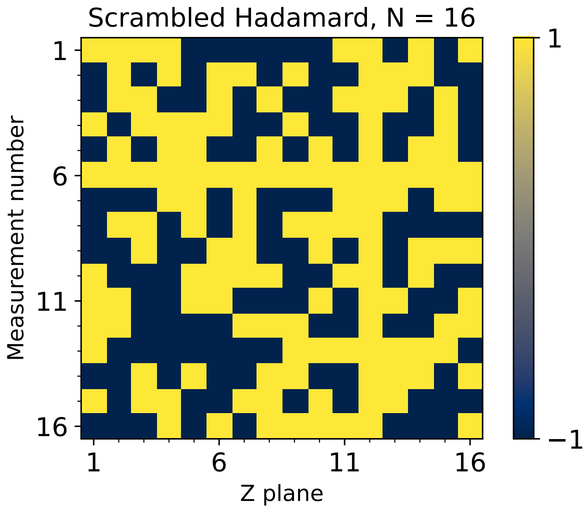

Figure 3.2: **Scrambled Hadamard patterns.** This matrix is a random row and column permutation of H_{16}.

3.3. Acquisition methods

We performed simulations of the direct and inverse problems to understand how *Single Frame* and *Double Frame* reconstructions compared to one another in terms of resiliency to noise and to sample movement. Data sets used in this section are complete, that is, we did not apply any Compressive sensing methods.

Figure 3.3 shows the measurement matrix we created to sample the unknown distribution $\boldsymbol{x}$ of Fig. 3.4. With these elements we simulated the direct problem and we obtained the spectra of Fig.3.5. This figure shows the raw data sets $\boldsymbol{y}$ for *Single Frame* and *Double Frame* acquisitions. As we expected, the *Single Frame* spectrum only exhibited positive values.

We reconstructed negative values in the *Single Frame* spectrum to explore what would happen. In particular, we subtracted from each raw data $\boldsymbol{y}$ the average of the measures y_m that were acquired with high spatial frequency patterns. For Walsh patterns, we performed this operation by subtracting the average of the values y_m for $m \geqslant l$. We empirically set $l = 7$ when $N = 16$. We found out that the resulting spectrum (called *Single Frame shifted* in Fig. 3.5) faithfully overlapped with the *Double Frame* spectrum.

At this point, we had simulated our measurements and we could proceed to solve the inverse problem just like we would after real experiments.

The least square solutions for the noiseless acquisitions are shown in Fig. 3.6. For simplicity's sake, we decided to apply Eq. 3.2 without any regularization term. The matrices

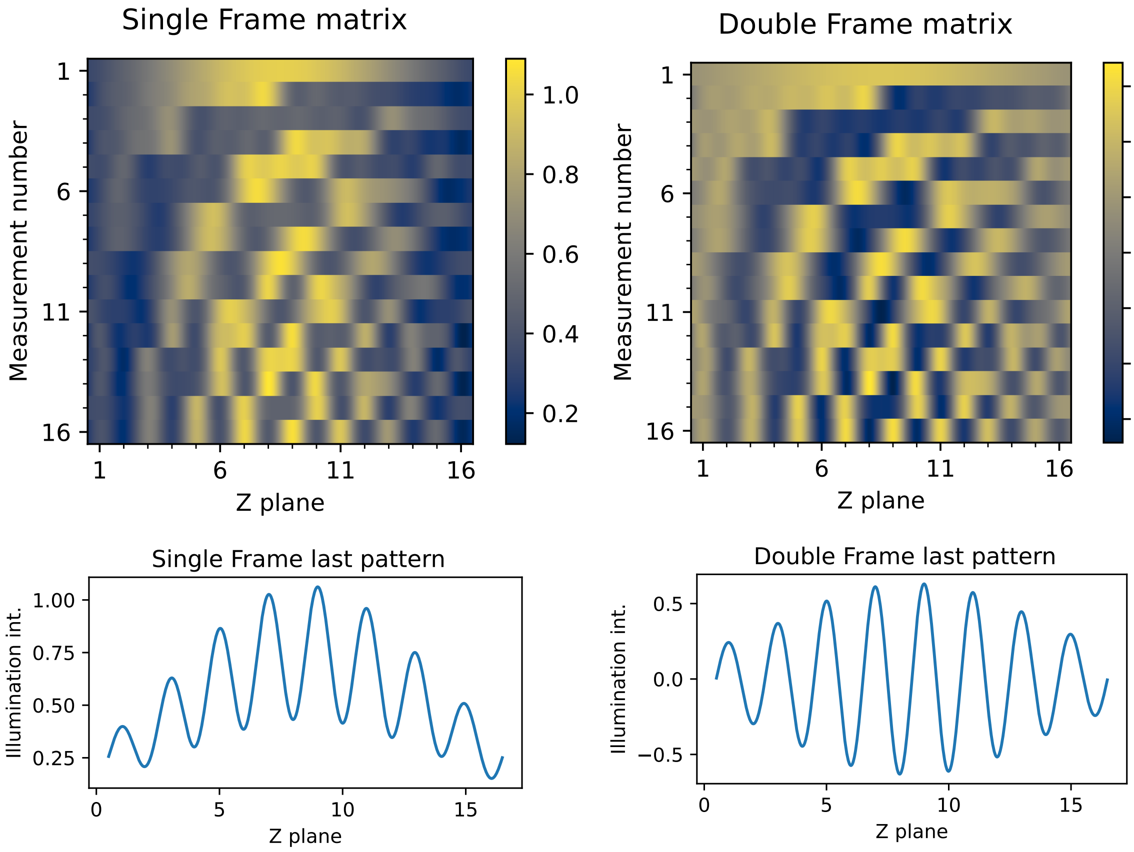

Figure 3.3: **Simulated direct problem matrices: Walsh-Hadamard.** Models of the pattern projected onto the sample. In the upper left corner we show a Walsh matrix where negative entries were removed. Moreover, to mimic the profile of Fig. 2.4, each row was modulated by a non uniform background and passed through a spatial low pass filter (operation that in reality is performed by the limited NA of the illumination objective). The upper right *Double Frame* matrix was obtained through the process described in Eq. 3.4 and was never used for the simulation of the direct problem.

used for the inverse problem were:

- The Walsh matrix with ±1s for *Double Frame* data sets and *Single Frame* data sets where negative values were reconstructed.
- The Walsh matrix with negative values set to zero for the *Single Frame* data set.

The biggest artifact we found was the abnormally high value in $Z = 1$ of the *Single Frame* reconstruction. Nevertheless, we found out that the reconstruction of negative values managed to solve this problem.

The divergence in the first plane is a consequence of the different fill factor (equal to 1) of

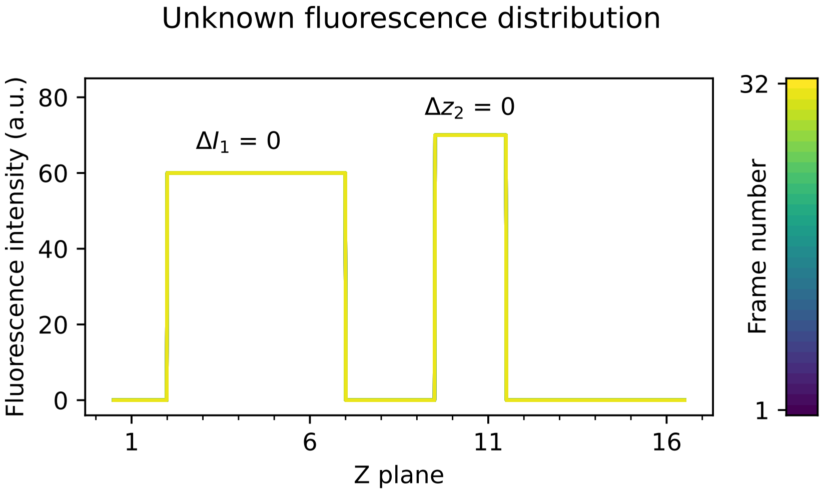

Figure 3.4: **Unknown Z fluorescence distribution.** In this case the distribution did not change with time. Over the 32 frames needed for a *Double Frame* acquisition, ΔI_1 represented the relative intensity variation of the left structure and Δz_2 represented the translation along Z of the right-hand structure expressed as fraction of the 16px Z range.

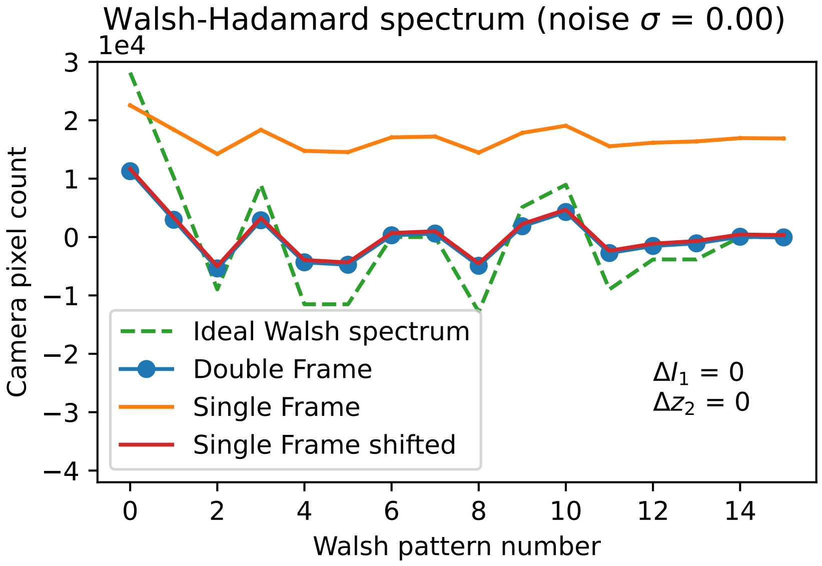

Figure 3.5: **Measured noiseless Walsh spectra of a non-moving object.** The ideal Walsh spectrum is the theoretical reference obtained with H_{16} as direct matrix.

the first pattern. We discarded the measurement of the first pattern and we inverted with $M = N - 1$ measurements to obtain the *Single Frame, no cc* curve. This curve shows a vertical displacement because it was built without knowledge on the total fluorescence along Z (given by the first pattern). For comparison, Fig. 3.7 shows the raw data of a SPIM acquisition with 16 planes.

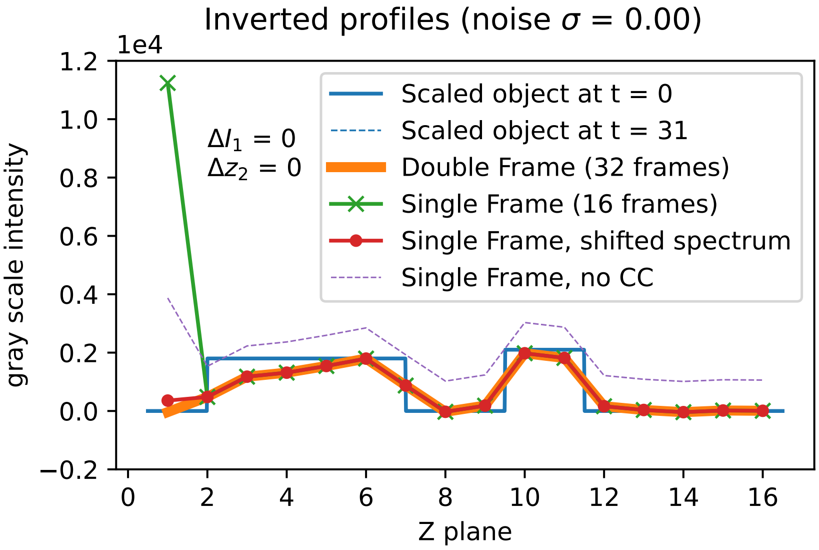

Figure 3.6: **Inverted profile of noiseless Walsh spectra of a non-moving object.**

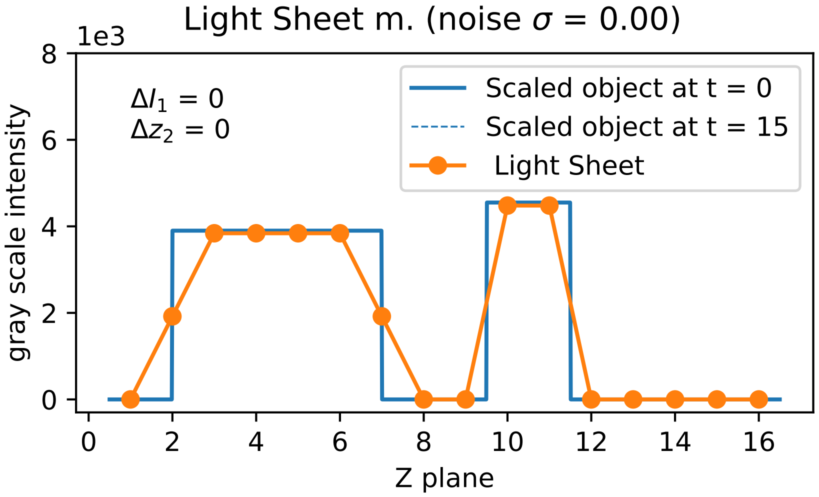

Figure 3.7: **Noiseless Light Sheet measurement of non-moving object.**

For more realistic simulations, we introduced multiplicative Gaussian noise in the measuring process (which was found to be dominant over additive noise [30]). With multiplicative noise, each value $y_m^{noise} = y_m \cdot e$, where e was normally distributed around $\mu = 1$ with standard deviation σ (Fig. 3.8).

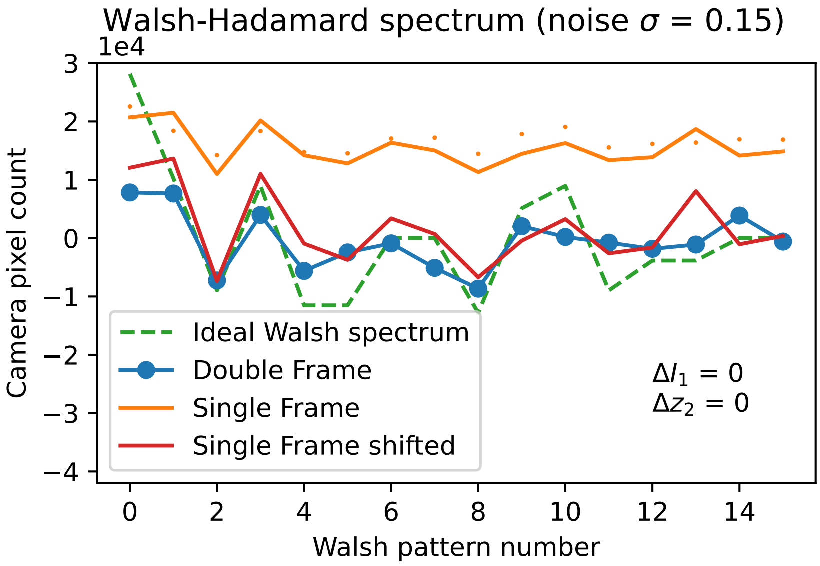

Figure 3.8: **Measured noisy Walsh spectra of a non-moving object.** Both the *Single Frame* and *Double Frame* spectra underwent multiplicative Gaussian noise. The orange dots show the noiseless *Single Frame* spectrum.

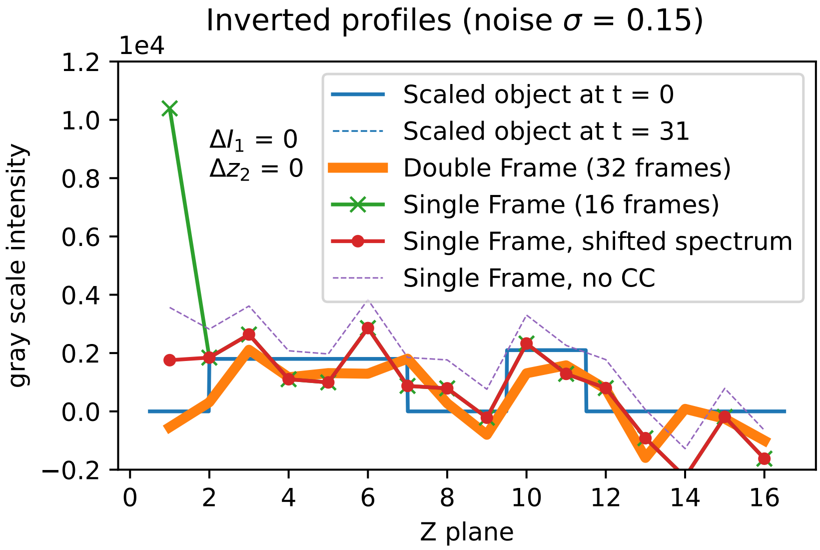

Figure 3.9: **Inverted profile of noisy Walsh spectrum of a non-moving object.**

Figure 3.9 shows how noise alters the shape of the reconstructed object and how negative values artifacts began to affect the reconstruction. We found out that the *Double Frame* inversion was more robust against noise as its signal to noise ratio is $\sqrt{2}$ times higher than that of *Single Frame* acquisition.

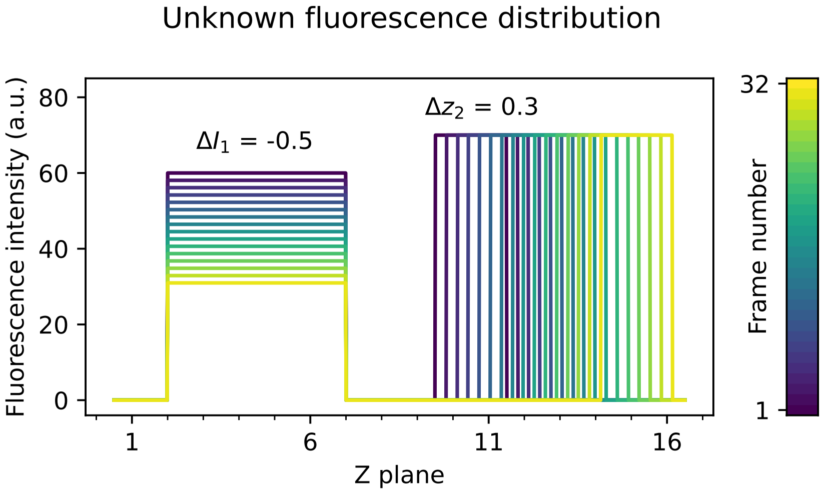

Figure 3.10: **Unknown Z fluorescence distribution with bleaching and translation.** We show the evolution of the sample during the acquisition of 32 frames.

To perform simulations closer to reality we used a dynamic object with fluorophore photobleaching and internal translation within the acquisition time of a single volume (Fig. 3.10). The direct problem was reformulated as $\boldsymbol{y} = \mathrm{diag}(\boldsymbol{\Phi} \cdot \boldsymbol{X})$ where $\boldsymbol{X}$ is a $N \times M$ matrix whose columns show the unknown object $\boldsymbol{x}$ at different times. *Double Frame* acquisitions used the whole temporal range, that is 32 object configurations, while *Single Frame* data set only witnessed the first 16. ΔI_1 was the relative intensity variation of the left structure and Δz_2 was the translation along Z of the right-hand structure (expressed as fraction of the Z range).

We found that the translation of the second peak produced artifacts in both *Single Frame* and *Double Frame* inversions (Fig. 3.11, mostly at the borders of the Z range). Even if the *Double Frame* data set witnessed twice as much movement, its inverted profile had an amount of artifacts comparable with the *Single Frame* profile. On the other hand, we saw that the bleaching of the first peak created significantly more problems in the *Single Frame* acquisition (Fig. 3.12). Finally, Fig. 3.13 shows the simultaneous effect of noise, sample bleaching and sample translation.

For comparison, we also used SPIM on the dynamic object: Fig. 3.14 shows the resulting distorted profile. In reality we have no way of knowing if it faithfully shows a motionless object or it is a misrepresentation of a moving object.

In conclusion, through this simulation we found that it is better to reconstruct negative values in *Single Frame* data sets and that *Double Frame* data sets are more resilient to noise but suffer more from sample movement.

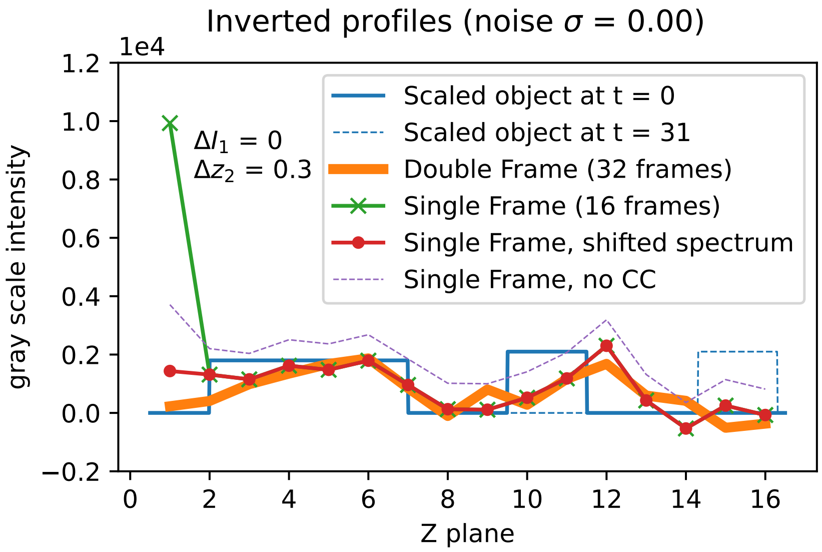

Figure 3.11: **Inverted profile of noiseless Walsh spectrum of a translating object.**

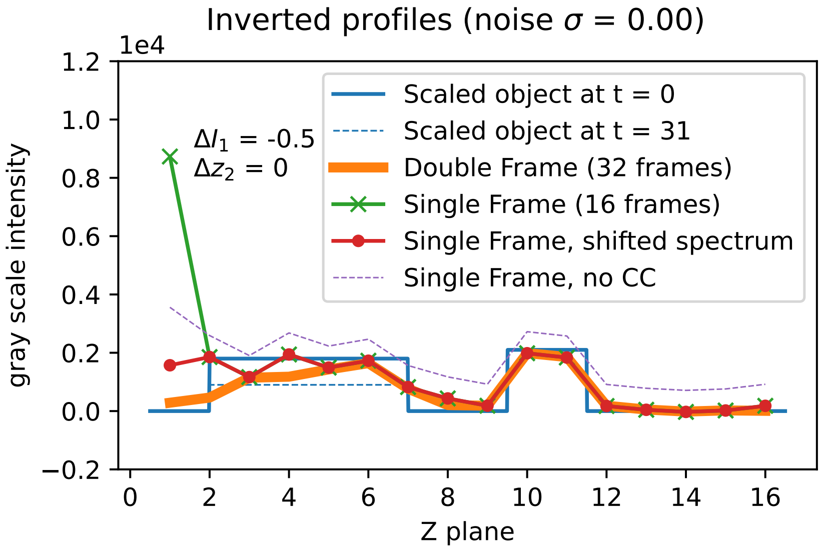

Figure 3.12: **Inverted profile of noiseless Walsh spectrum of an object with fluorophore bleaching.**

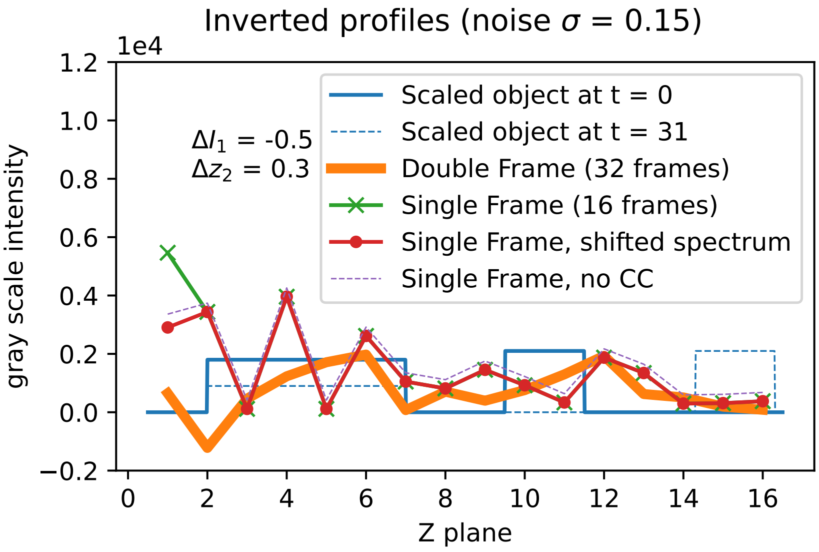

Figure 3.13: **Inverted profile of noisy Walsh spectrum of an object subject to bleaching and internal translation.**

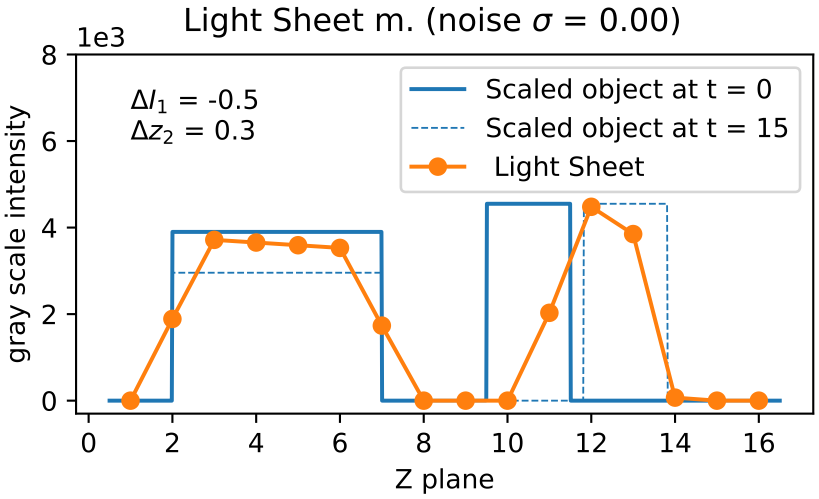

Figure 3.14: **Noiseless Light Sheet measurement of an evolving object.**

3.4. Compressed Sensing in 4D imaging

Time lapse measurements can really take advantage of Compressed sensing as they can use temporal regularization to reconstruct volumes that otherwise are too undersampled to be independently used.

So far, we have used $\boldsymbol{x}_{(i,j)} \in \mathbb{R}^N$ to independently describe the unknown Z fluorescence distributions in front of every (i,j) camera pixel in a given time point. If the camera sensor has n_V rows and n_H columns, $i = 1, \ldots, n_V$ and $j = 1, \ldots, n_H$.

Instead, if we want to reconstruct a compressed sensing 4D sampling, we need to promote spatial and temporal regularity over the whole time lapse. To handle the complete time series, let us define $\boldsymbol{x}^t \in \mathbb{R}^{(N \cdot n_V \cdot n_H)}$ as the column vector built by vertically stacking all the $\boldsymbol{x}_{(i,j)}$ of a given time point $t = 1, \ldots, T$ (where T is the total number of volumetric time points). Moreover, let us define a column vector $\hat{\boldsymbol{x}} \in \mathbb{R}^{(N \cdot n_V \cdot n_H \cdot T)}$ built by vertically stacking the different time points $\boldsymbol{x}^t$ $(\forall\ t = 1, \ldots, T)$.

It is also be useful to arrange the dynamic sample $\hat{\boldsymbol{x}}$ in a *Casorati* matrix $\mathrm{C}(\hat{\boldsymbol{x}})$. By definition, the columns of this matrix are the different time points:

$$\mathrm{C}(\hat{\boldsymbol{x}}) \equiv [\boldsymbol{x}^1,\ \boldsymbol{x}^2, \ldots,\ \boldsymbol{x}^T] \in \mathbb{R}^{(N \cdot n_V \cdot n_H)\ \times\ T}. \tag{3.5}$$

The measurement matrix $\hat{\boldsymbol{\Phi}}$ that we apply to $\hat{\boldsymbol{x}}$ is a block diagonal matrix built by repeating $n_V \cdot n_H$ times the measurement matrices $\boldsymbol{\Phi}_t \in \mathbb{R}^{M \times N}$ of each time point t. This way, the direct problem is defined for the whole time series but each $\boldsymbol{x}_{(i,j)} \in \mathbb{R}^N$ is still independently measured. For example, if $n_V \cdot n_H = 2$ and $T = 3$, the resulting measurement matrix is given by:

$$\hat{\boldsymbol{\Phi}} = \begin{bmatrix} \boldsymbol{\Phi}_1 & & & & & \\ & \boldsymbol{\Phi}_1 & & \mathbf{0} & & \\ & & \boldsymbol{\Phi}_2 & & & \\ & & & \boldsymbol{\Phi}_2 & & \\ & \mathbf{0} & & & \boldsymbol{\Phi}_3 & \\ & & & & & \boldsymbol{\Phi}_3 \end{bmatrix}. \tag{3.6}$$

The complete measured data $\hat{\boldsymbol{y}} = \hat{\boldsymbol{\Phi}} \cdot \hat{\boldsymbol{x}}$ is structured in the same way as $\hat{\boldsymbol{x}}$.

While Calisesi et al. [16] exclusively exploited spatial redundancies to reconstruct an undersampled volume, Tourais et al. [31] extended the hypothesis of sample regularity to the temporal dimension and were able to reconstruct compressed magnetic resonance dynamic images. In particular they used the alternating direction method of multipliers

(ADMM) to solve the following problem:

$$\underset{\hat{\boldsymbol{x}}}{\operatorname{argmin}}\Big(\left\|\hat{\boldsymbol{y}}-\hat{\boldsymbol{\Phi}}\cdot\hat{\boldsymbol{x}}\right\|_{l_2}^2+\alpha\left\|\mathrm{C}(\hat{\boldsymbol{x}})\right\|_*+\beta\left\|\mathrm{TV}(\hat{\boldsymbol{x}})\right\|_{l_1}\Big). \tag{3.7}$$

The two regularization terms respectively promote regularity in time and in space (with α and β as regularization parameters).

The regularization over time was built on the hypothesis that time points are mutually correlated because they follow a sufficiently slow movement of a given structure. Formally, this redundancy generates a *Low rank Casorati* matrix of the sample. We enforce this constraint by minimizing the sum of the singular values (that is, the nuclear norm $\|\bullet\|_*$) of $\mathrm{C}(\hat{\boldsymbol{x}})$.

On the other hand, spatial regularization is introduced by minimizing the anisotropic *Total Variation* of the sample: $\|\mathrm{TV}(\hat{\boldsymbol{x}})\|_{l_1} \equiv \|\nabla_x\hat{\boldsymbol{x}}\|_{l_1} + \|\nabla_y\hat{\boldsymbol{x}}\|_{l_1} + \|\nabla_z\hat{\boldsymbol{x}}\|_{l_1}$.

4 | Results

We proceeded to test the system on the zebrafish beating heart. The samples were prepared by the Department of Bioscience of the University of Milano following standard procedures. Decorionated specimen were delivered to us two days post fertilization.

We worked with zebrafish fluorescenct in the vasculature and blood cells. They were kept in 0.003% 1-phenyl-2-thiourea (PTU) to inhibit the melanization of tissues.

To reduce the movement of the fish during data set acquisition, we anesthetized samples by placing them in 0.016% tricaine (Ethyl 3-aminobenzoate methanesulfonate salt) and we restrained them in low melting point 2% agarose gel. The liquid gel with the sample was drawn in a capillary so that after its solidification we could extrude an agarose cylinder. During acquisitions, we lowered the sample in the cuvette which was filled with fish water (Instant Ocean, 0.1% Methylene Blue).

The *Zebrafish* or *Danio rerio* is one of the most used biological samples. It is a small fish coming from the rivers of northern India, Bangladesh and Nepal [32] (in Bengali *Danio* means “of the rice field” [33]). The zebrafish is an excellent model for accessing gene function in several human diseases; in particular, it can be used to study the cardiovascular system, both for congenital defects during embryological development and for drug screenings [34]. The zebrafish heart beats with a frequency of 2–4 Hz and has a dimension of circa 200 µm across [2].

4.1. Acquisition of complete data sets

We decided to test the system by acquiring complete data sets. In this way, we could retrospectively apply different types of data compression and optimize the reconstruction algorithms. We needed to verify that the system was fast enough to produce temporally correlated time points: if the sample moved too fast for our system, the hypothesis of temporal regularity would not stand (even for sped up compressed sensing acquisitions). Moreover, we wanted to investigate if introducing Low Rank temporal regularization offered substantial advantages over spatial regularization of individual time points.

Parameters	Description	
Fluorescent markers	KDRL + GATA	
Detection Objective	Nikon 20×, NA = 0.45	
Volume dimensions	X: 256 px · 0.339 µm/px = 86.8 µm Y: 2048 px · 0.339 µm/px = 694 µm Z: 16 px · 4.78 µm/px = 76.5 µm	
Laser power	40 mW	
Exposure time	1.208 ms	
Sensor read out time	1.388 ms	
Camera Frame rate	386.3 Hz	
Measurement matrix	$N = M = 16$ (no CS)	
	Single Frame	***Double Frame***
Frames per pattern	1	2
Frames per volume	16	32
Time per volume	41.41 ms	82.82 ms
Distance between time points	41.41 ms	82.82 ms
Pattern type	Scrambled Hadamard with different permutation for each time point	
Max. number of time points	Limited by the total number of different patterns (max. 400)	

Table 4.1: **Experimental details for complete data sets.**

To implement incoherent sampling we used scrambled Hadamard matrices [35]. The patterns were created through a different random permutation of $\boldsymbol{H}_{16}$ for each time point.

At the beginning of the experiment we generated and uploaded to the DMD the complete sequence of patterns to be used throughout the time lapse. The DMD limits the total number of pattern that can be used to 400. As a result, also the number of time points is limited. For this reason, we could record as many as 25 *Single Frame* volumes and as many as 12 *Double Frame* volumes.

Table 4.1 reports the details of the experiments carried out without direct use of compressed sensing. We used Hadamard matrices with dimension $N = 16$. The patterns were displayed on the DMD with a binning equal to 4, making the voxel Z dimension equal to:

$$(4 \cdot \sqrt{2} \cdot 7.56\,\mu\text{m}) \;/\; M_{exp} = 4.78\,\mu\text{m}, \tag{4.1}$$

where 4 is the DMD binning, $\sqrt{2} \cdot 7.56\,\mu\text{m}$ is the diagonal length of a DMD pixel and $M_{exp} = 8.94$ is the experimental illumination magnification.

We used a laser power of 40 mW and a pattern rate of 386.3 Hz. As a result, we needed 41.41 ms to acquire the 16 camera frames that built a *Single Frame* volume. *Double Frame* acquisitions required 32 frames and therefore took twice as much to be completed (82.82 ms).

We analysed raw data sets to understand how much the heart moved during the acquisition time of a single volume. Figures 4.1 and 4.2 show color-coded Maximum Intensity Projections (MIPs) of raw time points of *Single Frame* and *Double Frame* acquisitions: among the different measures of each XY pixel, we display the one with the highest intensity. Each one of these maximum values is given a color based on its frame of origin. These Figures show that over the 32 frames used for *Double Frame* volumes, the heart movement was more pronounced than over the 16 frames of a *Single Frame* data set. As found in the simulations of chapter 3, sample movement during the acquisition of a time point creates artifacts in the reconstructed volume.

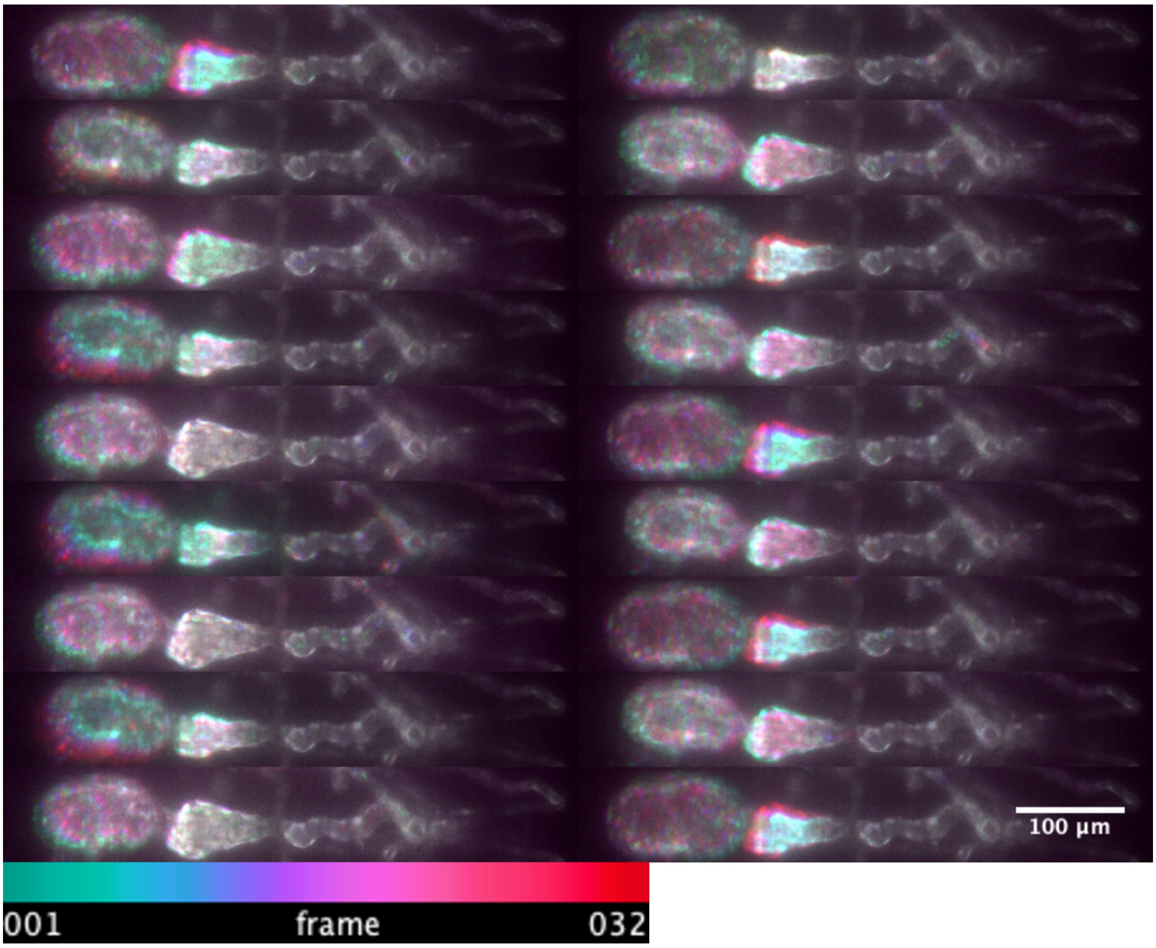

Figure 4.1: **Color-coded MIP of raw *Double Frame* data sets.** We show the color-coded MIP over the raw frames of 18 different time points of a time lapse acquired with the *Double Frame* method. Separation of color indicates movement of the heart between the first and last (i.e., 32^{nd}) frame.

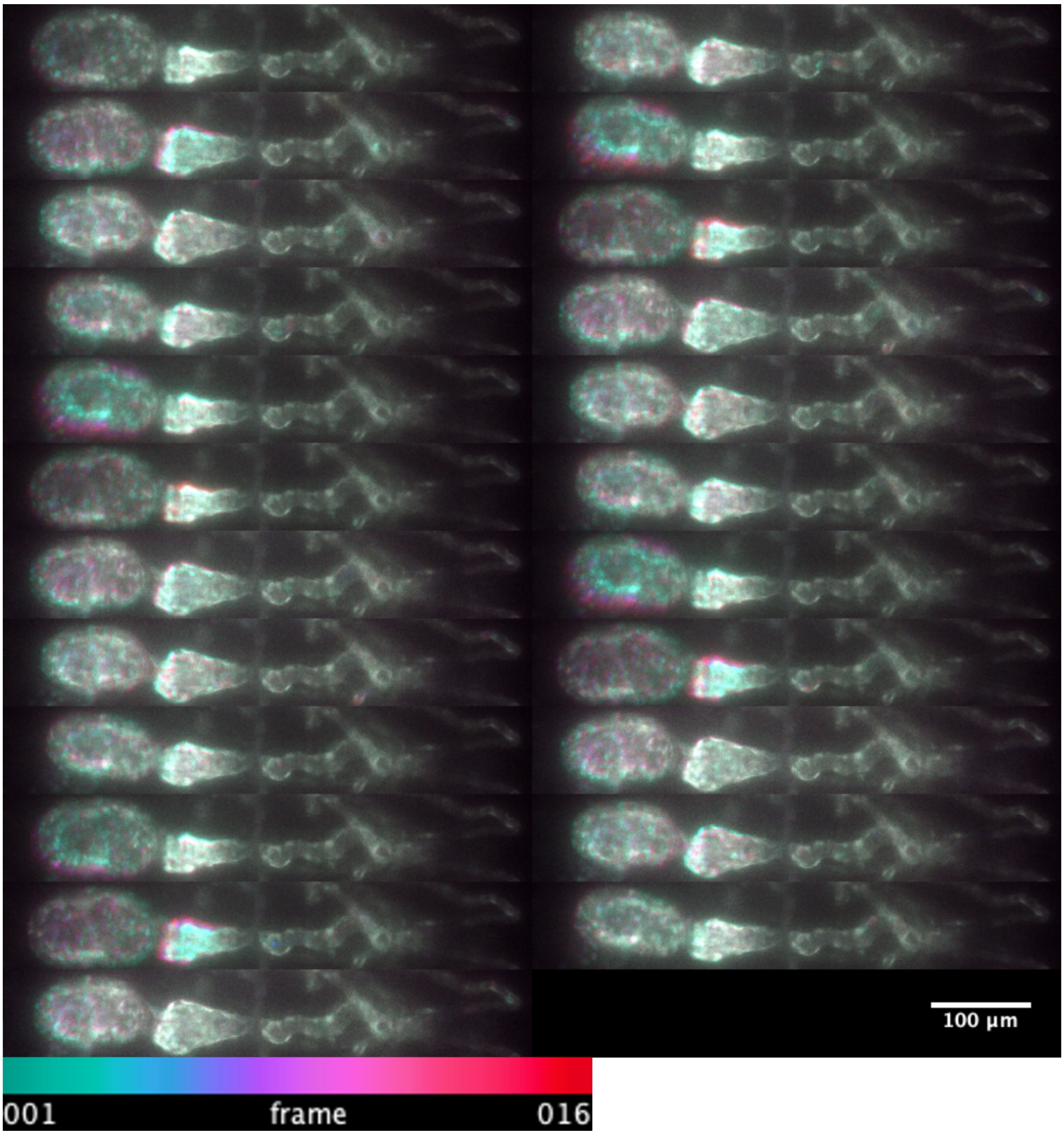

Figure 4.2: **Color-coded MIP of raw *Single Frame* data sets.** We show the color-coded MIP over the raw frames of 23 different time points of a time lapse acquired with the *Single Frame* method. Separation of color indicates movement of the heart between the first and last (i.e., 16^{th}) frame.

4.2. Inversion tests

To test the algorithms and the effect of Low Rank regularization we inverted the complete data sets in three ways:

- We used all the acquired frames ($M = N = 16$) to obtain a non-compressed reconstruction. In this case, we did not apply Low rank or Total Variation regularization ($\alpha = 0$ and $\beta = 0$ in Eq. 3.7)
- We performed an ex-post 2× compression and applied only Total Variation (TV, i.e. spatial) regularization. We discarded half of the acquired frames to bring $M = N/2 = 8$ and we used $\alpha \neq 0$ and $\beta = 0$ in Eq. 3.7.
- We performed an ex-post 2× compression and applied both spatial and temporal regularization (Low Rank). We discarded half of the acquired frames to bring $M = N/2 = 8$ and we used $\alpha \neq 0$ and $\beta \neq 0$ in Eq. 3.7.

In the case of retrospective compression, we had to make sure that we always used the measurement where the whole volume is illuminated (i.e., the Continuous Wave component, CW) as it gives the image contrast (without the CW we would just have edges).

Figures 4.3 and 4.4 show orthogonal sections and Maximum Intensity Projections (MIPs) of a *Double Frame* time point inverted with the three different methods. This results indicate that TV spatial regularization of independent volumes struggled to yield clean images (Fig. 4.3B) and that we needed time regularization to reconstruct the compressed time lapse (Fig. 4.3C). Using compression, $M = 16/CS_{ratio}$ becomes too small to independently reconstruct each volume (i.e., with $\alpha = 0$ in Eq. 3.7).

Around the upper heart chamber of Fig. 4.4C, we can see the effects of blurring between two time points: two shapes of the same structure are overlapping. This is due to the temporal regularization we imposed. We expect that this problem will be reduced when using prospectively compressed data: time points will get closer to each other and achieve higher temporal regularity.

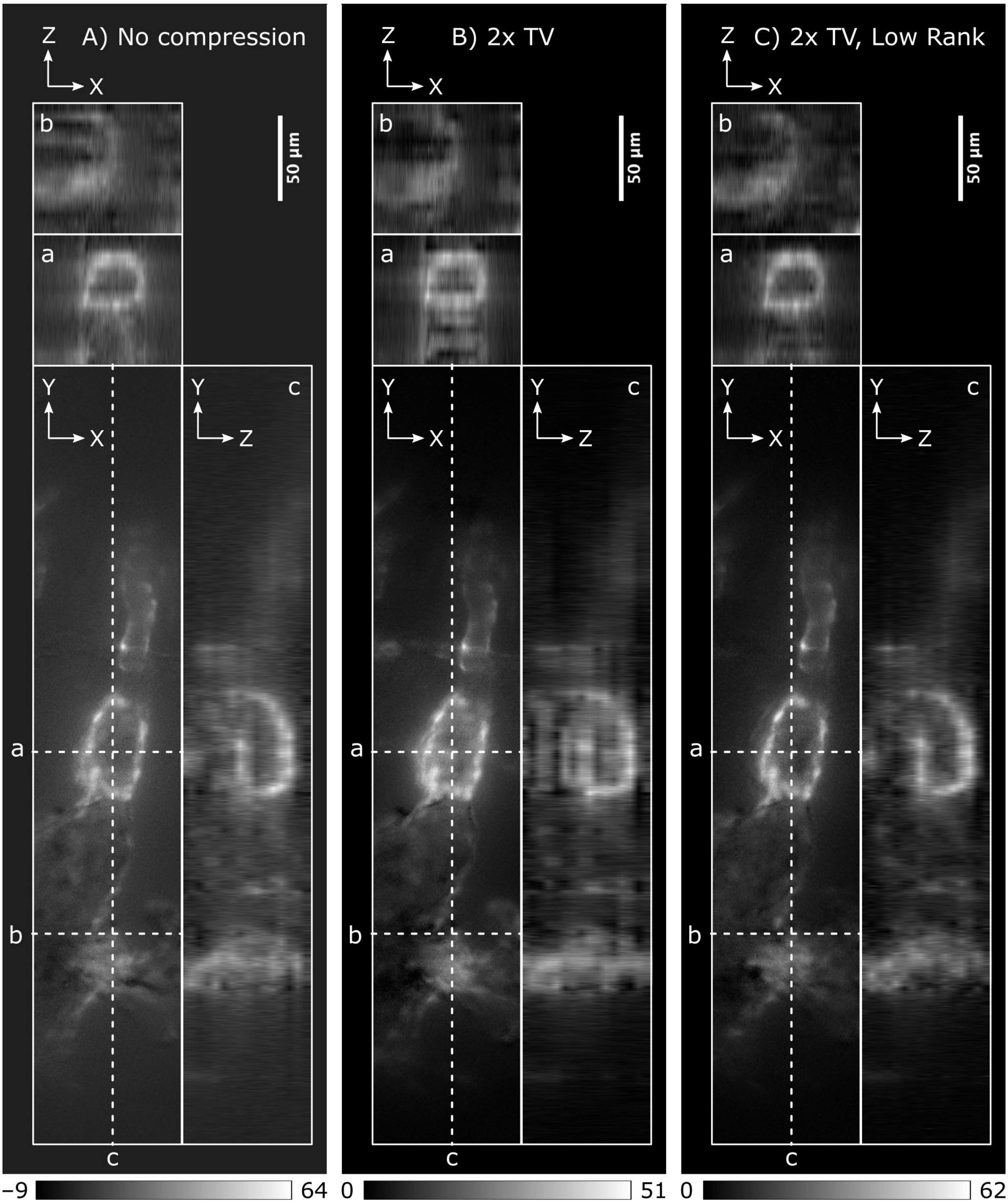

Figure 4.3: **Orthogonal sections of the zebrafish heart reconstructed with *Double Frame* data sets.** The inversions were performed: (A) using the complete data set, (B) discarding a posteriori half of the frames and imposing Total Variation (TV) regularization and, (C) discarding a posteriori half of the frames and imposing TV and Low Rank regularization. Dotted lines in the XY plane show the positions of the orthogonal sections reported in panels a, b and c.

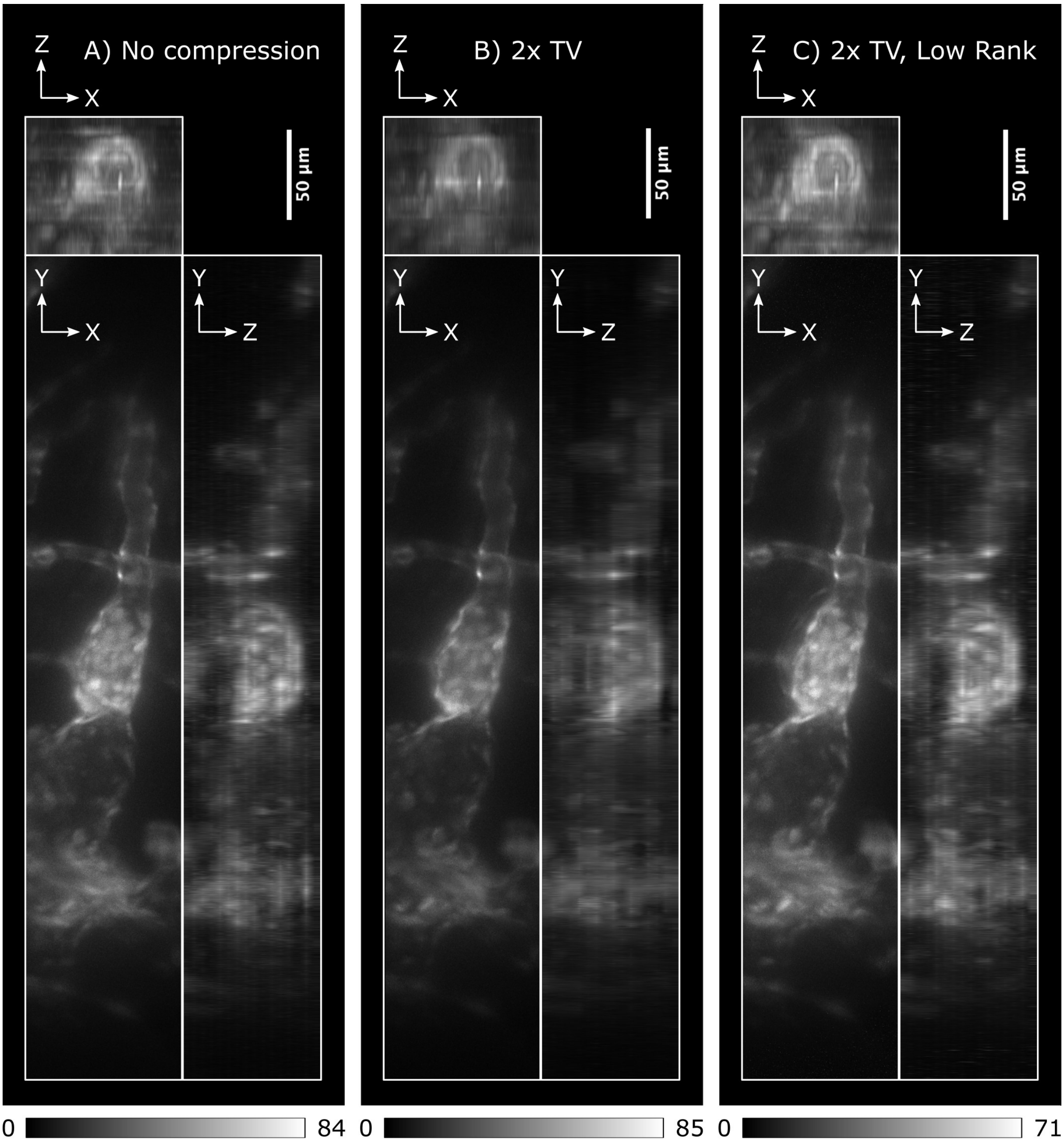

Figure 4.4: **Orthogonal Maximum Intensity Projections of the zebrafish heart reconstructed with *Double Frame* data sets.** The inversions were performed: (A) using the complete data set, (B) discarding a posteriori half of the frames and imposing Total Variation (TV) regularization and, (C) discarding a posteriori half of the frames and imposing TV and Low Rank regularization.

At this point we tested if we could improve the reconstruction by using the *Single Frame* scheme. In particular, we wanted to see the effects of cutting in half the acquisition time.

Figures 4.5 and 4.6 show orthogonal sections and projections of a *Single Frame* time point inverted with the three methods (i.e., complete set, ex-post 2× compression with TV and ex-post 2× compression with TV and Low Rank). These images generally showed crispier details than the *Double Frame* acquisition. However, they also had lower signal to noise ratio and strong planar artifacts (in different XY planes across different time points).

Figure 4.7 shows a reference volume reconstruction built using light sheet sectioning. With the DMD we produced a 4.78 µm thick light sheet and we moved it along the Z axis. This way, the voxels of these volumes are consistent with the voxels of the reconstructions shown so far.

In conclusion, experiments with complete data sets indicated that the camera frame rate was optimized for the application of compressed sensing and that we could use *Single Frame* acquisitions to speed up the process at the cost of a lower signal to noise ratio.

Moreover, we tested the acquisition and reconstruction requirements with noisy data and we found that Low Rank regularization was necessary to obtain good results when the number of measurements M for each volume was very small.

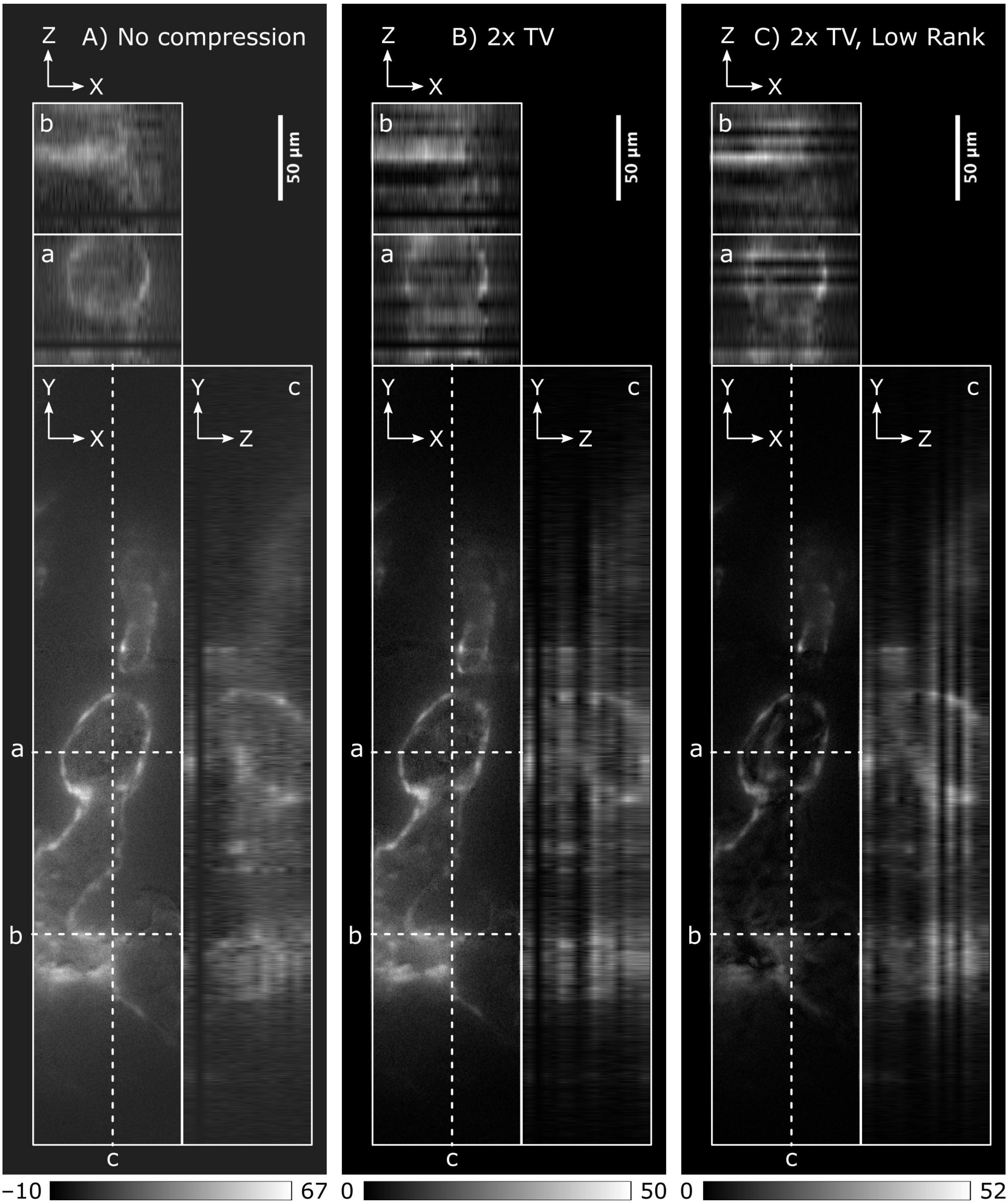

Figure 4.5: **Orthogonal sections of the zebrafish heart acquired in *Single Frame* mode.** The inversions were performed: (A) using the complete data set, (B) discarding a posteriori half of the frames and imposing Total Variation (TV) regularization and, (C) discarding a posteriori half of the frames and imposing TV and Low Rank regularization.

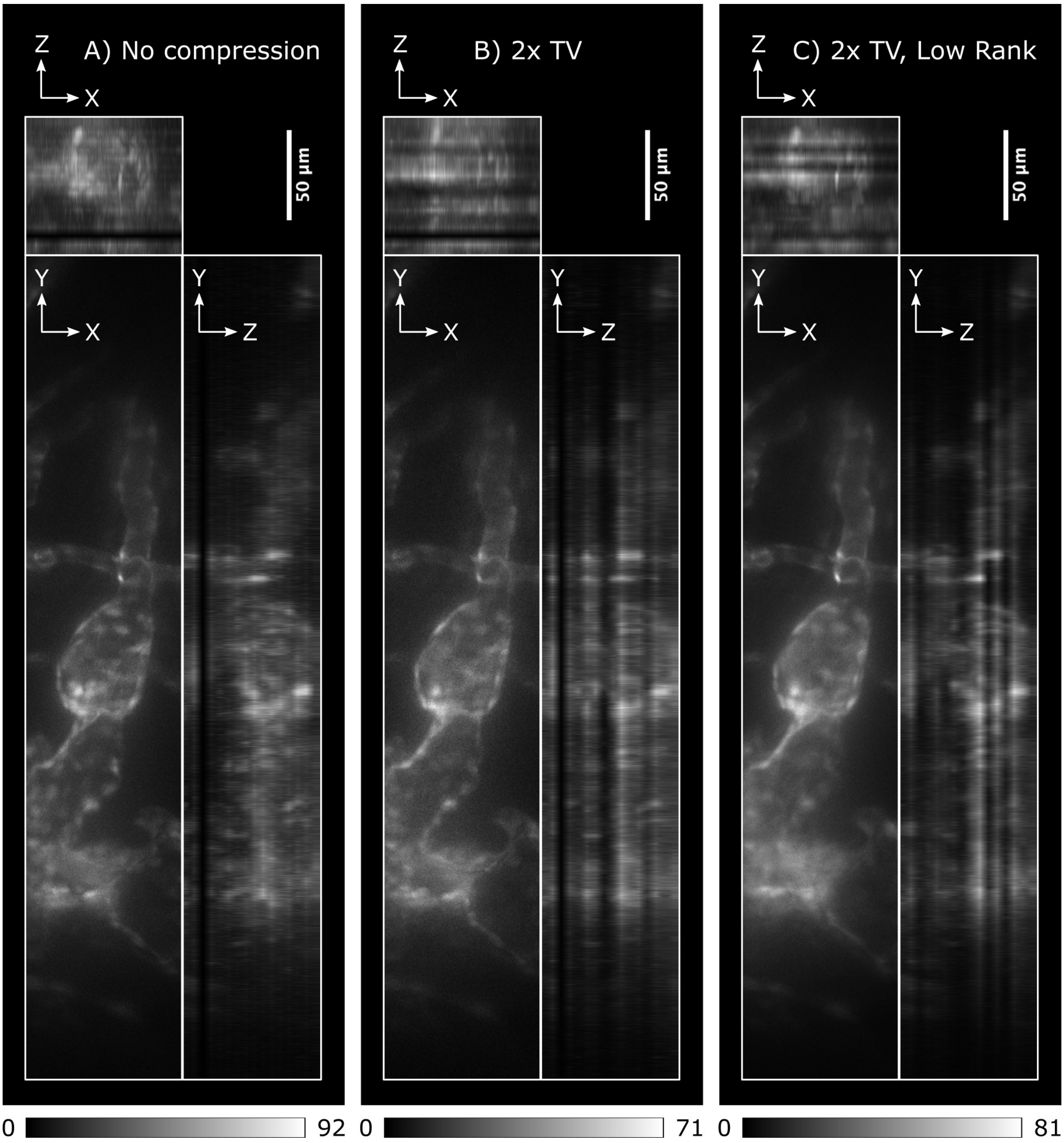

Figure 4.6: **Orthogonal MIPs of a zebrafish heart acquired in *Single Frame* mode.** he inversions were performed: (A) using the complete data set, (B) discarding a posteriori half of the frames and imposing Total Variation (TV) regularization and, (C) discarding a posteriori half of the frames and imposing TV and Low Rank regularization.

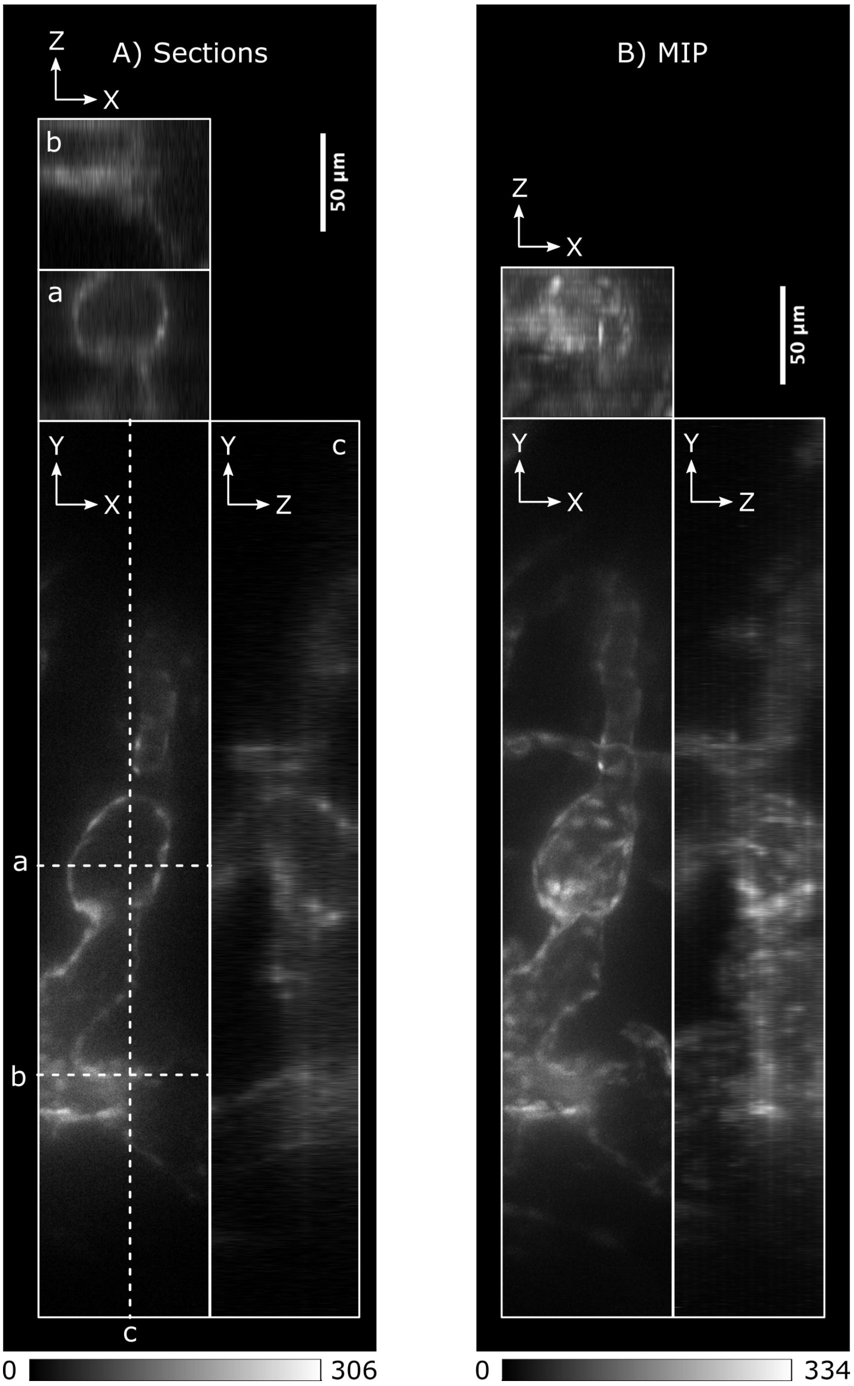

Figure 4.7: **Orthogonal views of a zebrafish heart acquired with a scanning light sheet.** Dotted lines in the XY plane of panel A show the positions of the orthogonal sections reported in panels a, b and c. Panel B shows the MIPs along the three axis.

5 | Conclusions

We built a new fluorescence microscopy setup to perform 4D imaging of dynamic samples with a time resolution of circa 40 ms, showing the possibility to achieve our goal. Starting from Light Sheet Fluorescence Microscopy and Spatially Modulated Selective Volume Illumination Microscopy we worked to implement Compresses Sensing and increase the volume sampling rate.

We optimized the system to reach frame rates previously not accessible in our laboratory. In particular, we payed close attention to hardware management: we used Python to control the DMD and the camera during experiments. The resulting acquisition time of a single volume was compatible with Low Rank compressed sensing: even without compression, the temporal resolution was sufficient to smoothly follow events that evolved on the millisecond time scale.

We experimented with different methodologies for the inversion of complete and retrospectively compressed data sets. We found that temporal regularization (with Low Rank) was pivotal for the reconstruction of time series that have few measurement for each volume. Based on our tests, in the future we expect to achieve better results with data sets that were compressed during data acquisition.

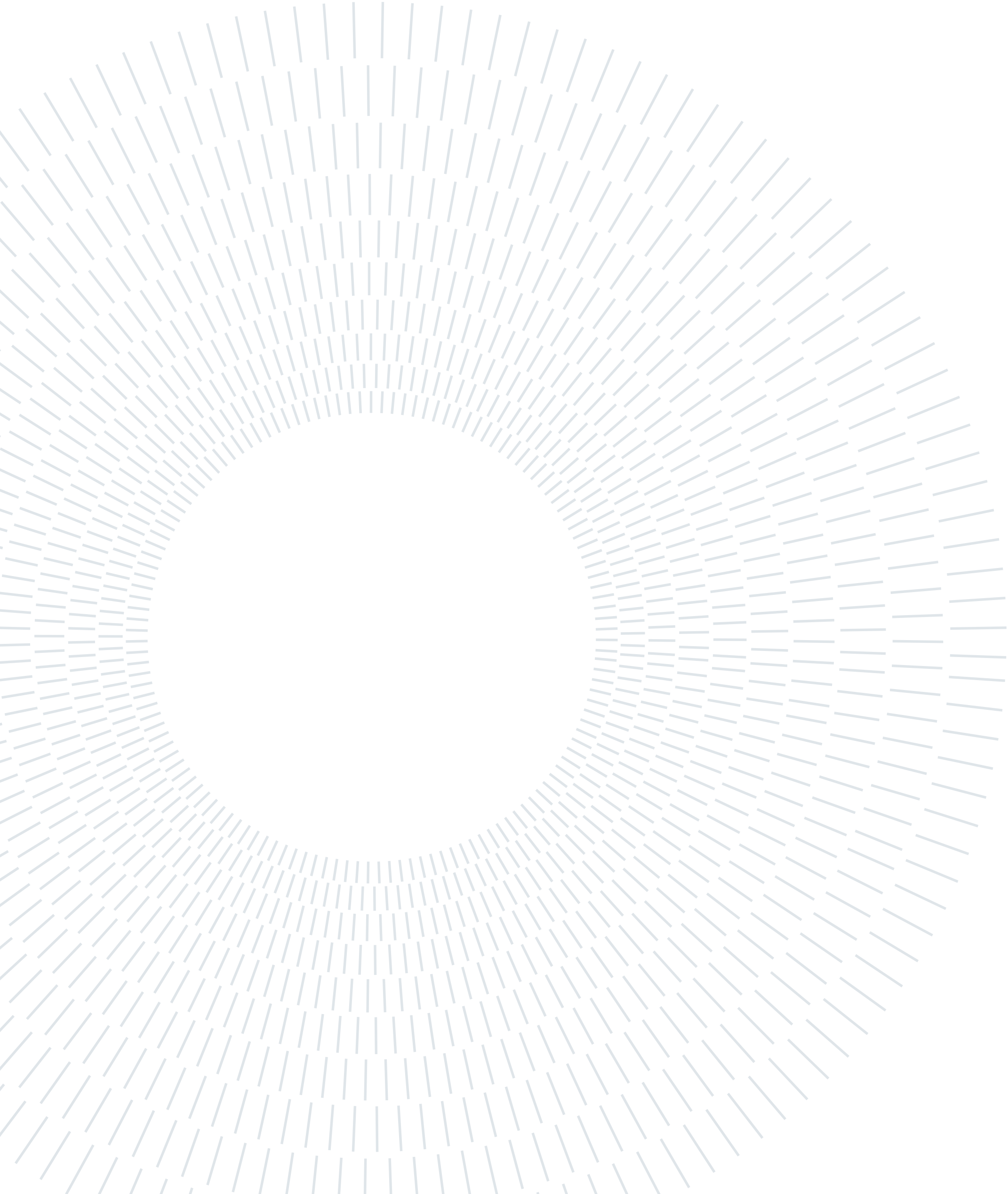

Bibliography

[1] J. Huisken and D. Y. R. Stainier, “Selective plane illumination microscopy techniques in developmental biology,” *Development*, vol. 136, no. 12, pp. 1963–1975, 06 2009. [Online]. Available: https://doi.org/10.1242/dev.022426

[2] F. O. Fahrbach, F. F. Voigt, B. Schmid, F. Helmchen, and J. Huisken, “Rapid 3d light-sheet microscopy with a tunable lens,” *Opt. Express*, vol. 21, no. 18, pp. 21 010–21 026, Sep 2013. [Online]. Available: https://opg.optica.org/oe/abstract.cfm?URI=oe-21-18-21010

[3] J. Huisken and D. Y. R. Stainier, “Even fluorescence excitation by multidirectional selective plane illumination microscopy (mspim),” *Opt. Lett.*, vol. 32, no. 17, pp. 2608–2610, Sep 2007. [Online]. Available: https://opg.optica.org/ol/abstract.cfm?URI=ol-32-17-2608

[4] J. Huisken, J. Swoger, F. D. Bene, J. Wittbrodt, and E. H. K. Stelzer, “Optical sectioning deep inside live embryos by selective plane illumination microscopy,” *Science*, vol. 305, no. 5686, pp. 1007–1009, 2004. [Online]. Available: https://www.science.org/doi/abs/10.1126/science.1100035

[5] M. Mickoleit, B. Schmid, M. Weber, F. O. Fahrbach, S. Hombach, S. Reischauer, and J. Huisken, “High-resolution reconstruction of the beating zebrafish heart,” *Nature Methods*, vol. 11, no. 9, pp. 919–922, 2014. [Online]. Available: https://doi.org/10.1038/nmeth.3037

[6] P. Fei, J. Lee, R. S. Packard, K.-I. Sereti, H. Xu, J. Ma, Y. Ding, H. Kang, H. Chen, K. Sung, R. Kulkarni, R. Ardehali, C. C. J. Kuo, X. Xu, C.-M. Ho, and T. K. Hsiai, “Cardiac light-sheet fluorescent microscopy for multi-scale and rapid imaging of architecture and function,” *Scientific Reports*, vol. 6, no. 1, p. 22489, 2016. [Online]. Available: https://doi.org/10.1038/srep22489

[7] L. Sacconi, L. Silvestri, E. C. Rodríguez, G. A. Armstrong, F. S. Pavone, A. Shrier, and G. Bub, “Khz-rate volumetric voltage imaging of the whole zebrafish

heart," *Biophysical Reports*, vol. 2, no. 1, p. 100046, 2022. [Online]. Available: https://www.sciencedirect.com/science/article/pii/S2667074722000039

[8] B.-C. Chen, W. R. Legant, K. Wang, L. Shao, D. E. Milkie, M. W. Davidson, C. Janetopoulos, X. S. Wu, J. A. Hammer, Z. Liu, B. P. English, Y. Mimori-Kiyosue, D. P. Romero, A. T. Ritter, J. Lippincott-Schwartz, L. Fritz-Laylin, R. D. Mullins, D. M. Mitchell, J. N. Bembenek, A.-C. Reymann, R. Böhme, S. W. Grill, J. T. Wang, G. Seydoux, U. S. Tulu, D. P. Kiehart, and E. Betzig, "Lattice light-sheet microscopy: Imaging molecules to embryos at high spatiotemporal resolution," *Science*, vol. 346, no. 6208, p. 1257998, 2014. [Online]. Available: https://www.science.org/doi/abs/10.1126/science.1257998

[9] K. M. Dean, P. Roudot, E. S. Welf, T. Pohlkamp, G. Garrelts, J. Herz, and R. Fiolka, "Imaging subcellular dynamics with fast and light-efficient volumetrically parallelized microscopy," *Optica*, vol. 4, no. 2, pp. 263–271, Feb 2017. [Online]. Available: https://opg.optica.org/optica/abstract.cfm?URI=optica-4-2-263

[10] Y.-X. Ren, J. Wu, Q. T. K. Lai, H. M. Lai, D. M. D. Siu, W. Wu, K. K. Y. Wong, and K. K. Tsia, "Parallelized volumetric fluorescence microscopy with a reconfigurable coded incoherent light-sheet array," *Light: Science & Applications*, vol. 9, no. 1, p. 8, 2020. [Online]. Available: https://doi.org/10.1038/s41377-020-0245-8

[11] M. B. Bouchard, V. Voleti, C. S. Mendes, C. Lacefield, W. B. Grueber, R. S. Mann, R. M. Bruno, and E. M. C. Hillman, "Swept confocally-aligned planar excitation (scape) microscopy for high-speed volumetric imaging of behaving organisms," *Nature Photonics*, vol. 9, no. 2, pp. 113–119, 2015. [Online]. Available: https://doi.org/10.1038/nphoton.2014.323

[12] V. Voleti, K. B. Patel, W. Li, C. Perez Campos, S. Bharadwaj, H. Yu, C. Ford, M. J. Casper, R. W. Yan, W. Liang, C. Wen, K. D. Kimura, K. L. Targoff, and E. M. C. Hillman, "Real-time volumetric microscopy of in vivo dynamics and large-scale samples with scape 2.0," *Nature Methods*, vol. 16, no. 10, pp. 1054–1062, 2019. [Online]. Available: https://doi.org/10.1038/s41592-019-0579-4

[13] G. Calisesi, A. Ghezzi, D. Ancora, C. D'Andrea, G. Valentini, A. Farina, and A. Bassi, "Compressed sensing in fluorescence microscopy," *Progress in Biophysics and Molecular Biology*, vol. 168, pp. 66–80, 2022. [Online]. Available: https://www.sciencedirect.com/science/article/pii/S007961072100064X

[14] E. J. Candes and M. B. Wakin, "An introduction to compressive sampling," *IEEE Signal Processing Magazine*, vol. 25, no. 2, pp. 21–30, 2008.

[15] R. Tomer, M. Lovett-Barron, I. Kauvar, A. Andalman, V. M. Burns, S. Sankaran, L. Grosenick, M. Broxton, S. Yang, and K. Deisseroth, "Sped light sheet microscopy: Fast mapping of biological system structure and function," *Cell*, vol. 163, no. 7, pp. 1796–1806, 2022/10/06 2015. [Online]. Available: https://doi.org/10.1016/j.cell.2015.11.061

[16] G. Calisesi, M. Castriotta, A. Candeo, A. Pistocchi, C. D'Andrea, G. Valentini, A. Farina, and A. Bassi, "Spatially modulated illumination allows for light sheet fluorescence microscopy with an incoherent source and compressive sensing," *Biomed. Opt. Express*, vol. 10, no. 11, pp. 5776–5788, Nov 2019. [Online]. Available: http://opg.optica.org/boe/abstract.cfm?URI=boe-10-11-5776

[17] [Online]. Available: https://spectrum.ieee.org/chip-hall-of-fame-texas-instruments-digital-micromirror-device

[18] A. Travinsky, D. Vorobiev, Z. Ninkov, A. Raisanen, M. A. Quijada, S. A. Smee, J. A. Pellish, T. Schwartz, M. Robberto, S. Heap, D. Conley, C. Benavides, N. Garcia, Z. Bredl, and S. Yllanes, "Evaluation of digital micromirror devices for use in space-based multiobject spectrometer application," *Journal of Astronomical Telescopes, Instruments, and Systems*, vol. 3, no. 03, p. 1, aug 2017. [Online]. Available: https://doi.org/10.1117%2F1.jatis.3.3.035003

[19] P. Ricci, V. Gavryusev, C. Müllenbroich, L. Turrini, G. de Vito, L. Silvestri, G. Sancataldo, and F. S. Pavone, "Removing striping artifacts in light-sheet fluorescence microscopy: a review," *Progress in Biophysics and Molecular Biology*, vol. 168, pp. 52–65, 2022, the Resolution Revolution: Fluorescence Microscopy of Biological Samples from Micro to Meso. [Online]. Available: https://www.sciencedirect.com/science/article/pii/S0079610721000821

[20] J. Mertz, *Introduction to Optical Microscopy*, 2nd ed. Cambridge University Press, 2019.

[21] M. G. Gustafsson, L. Shao, P. M. Carlton, C. J. R. Wang, I. N. Golubovskaya, W. Z. Cande, D. A. Agard, and J. W. Sedat, "Three-dimensional resolution doubling in wide-field fluorescence microscopy by structured illumination," *Biophysical Journal*, vol. 94, no. 12, pp. 4957–4970, 2008. [Online]. Available: https://www.sciencedirect.com/science/article/pii/S0006349508703606

[22] P. T. Brown, R. Kruithoff, G. J. Seedorf, and D. P. Shepherd, "Multicolor structured illumination microscopy and quantitative control of polychromatic light with a digital micromirror device." *Biomed Opt Express*, vol. 12, no. 6, pp. 3700–3716, Jun 2021.

[23] Texas Instruments, *Using Lasers with DLP® DMD technology*, Sep 2008. [Online]. Available: https://www.ti.com/lit/wp/dlpa037/dlpa037.pdf

[24] M. Lachetta, H. Sandmeyer, A. Sandmeyer, J. S. a. Esch, T. Huser, and M. Müller, "Simulating digital micromirror devices for patterning coherent excitation light in structured illumination microscopy," *Philosophical Transactions of the Royal Society A: Mathematical, Physical and Engineering Sciences*, vol. 379, no. 2199, p. 20200147, 2021. [Online]. Available: https://royalsocietypublishing.org/doi/abs/10.1098/rsta.2020.0147

[25] M. Lachetta, G. Wiebusch, W. Hübner, J. S. am Esch, T. Huser, and M. Müller, "Dual color dmd-sim by temperature-controlled laser wavelength matching," *Opt. Express*, vol. 29, no. 24, pp. 39 696–39 708, Nov 2021. [Online]. Available: https://opg.optica.org/oe/abstract.cfm?URI=oe-29-24-39696

[26] Hamamatsu Photonics K.K., *Digital Camera C11440-22CU/C11440-22CU01 Instruction manual v.1.4*, Jul 2014.

[27] Texas Instruments, *DLPC900 Programmer's Guide, DLPU018G*, Apr 2022.

[28] [Online]. Available: http://www.scopefoundry.org

[29] M. Harwit and N. J. A. Sloan, *Hadamard Transform Optics*. Elsevier, 1979.

[30] P. Withagen, F. Groen, and K. Schutte, "Ccd characterization for a range of color cameras," in *2005 IEEE Instrumentationand Measurement Technology Conference Proceedings*, vol. 3, 2005, pp. 2232–2235.

[31] J. Tourais, C. M. Scannell, T. Schneider, E. Alskaf, R. Crawley, F. Bosio, J. Sanchez-Gonzalez, M. Doneva, C. Schülke, J. Meineke, J. Keupp, J. Smink, M. Breeuwer, A. Chiribiri, M. Henningsson, and T. Correia, "High-resolution free-breathing quantitative first-pass perfusion cardiac mr using dual-echo dixon with spatio-temporal acceleration," *Frontiers in Cardiovascular Medicine*, vol. 9, 2022. [Online]. Available: https://www.frontiersin.org/articles/10.3389/fcvm.2022.884221

[32] R. Spence, G. Gerlach, C. Lawrence, and C. Smith, "The behaviour and ecology of the zebrafish, danio rerio," *Biological Reviews*, vol. 83, no. 1, pp. 13–34, 2008. [Online]. Available: https://onlinelibrary.wiley.com/doi/abs/10.1111/j.1469-185X.2007.00030.x

[33] P. Talwar and A. Jhingran, *Inland Fishes of India and Adjacent Countries*, ser. Inland Fishes of India and Adjacent Countries. Oxford & IBH Publishing Company, 1991, no. v. 2.

[34] B. Tavares and S. S. Lopes, “The importance of zebrafish in biomedical research,” *Acta Médica Portuguesa*, vol. 26, no. 5, pp. 583–592, 2013. [Online]. Available: https://www.actamedicaportuguesa.com/revista/index.php/amp/article/view/4628

[35] M. Lustig, D. L. Donoho, J. M. Santos, and J. M. Pauly, “Compressed sensing mri,” *IEEE Signal Processing Magazine*, vol. 25, no. 2, pp. 72–82, 2008.

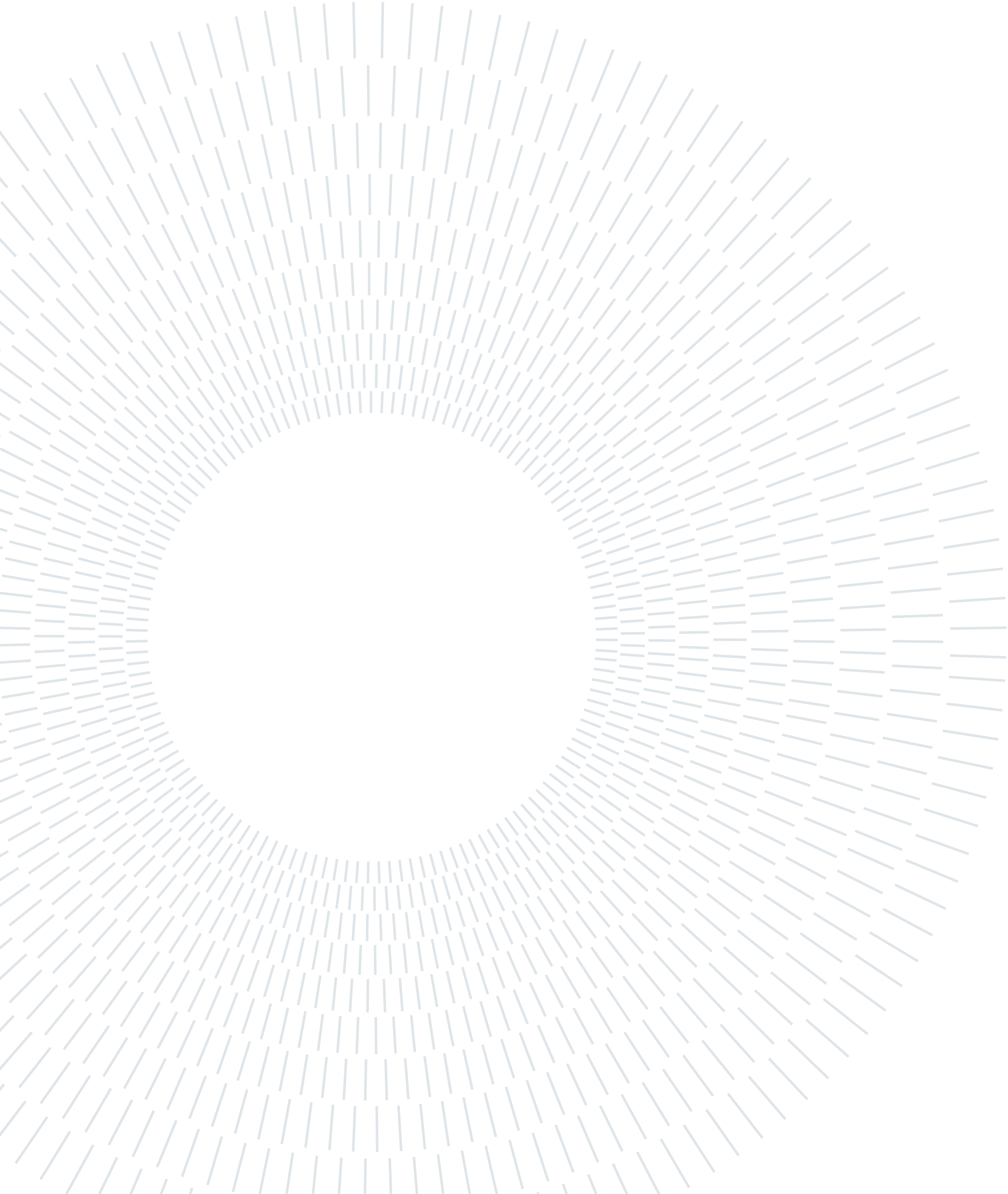

List of Figures

List of Tables

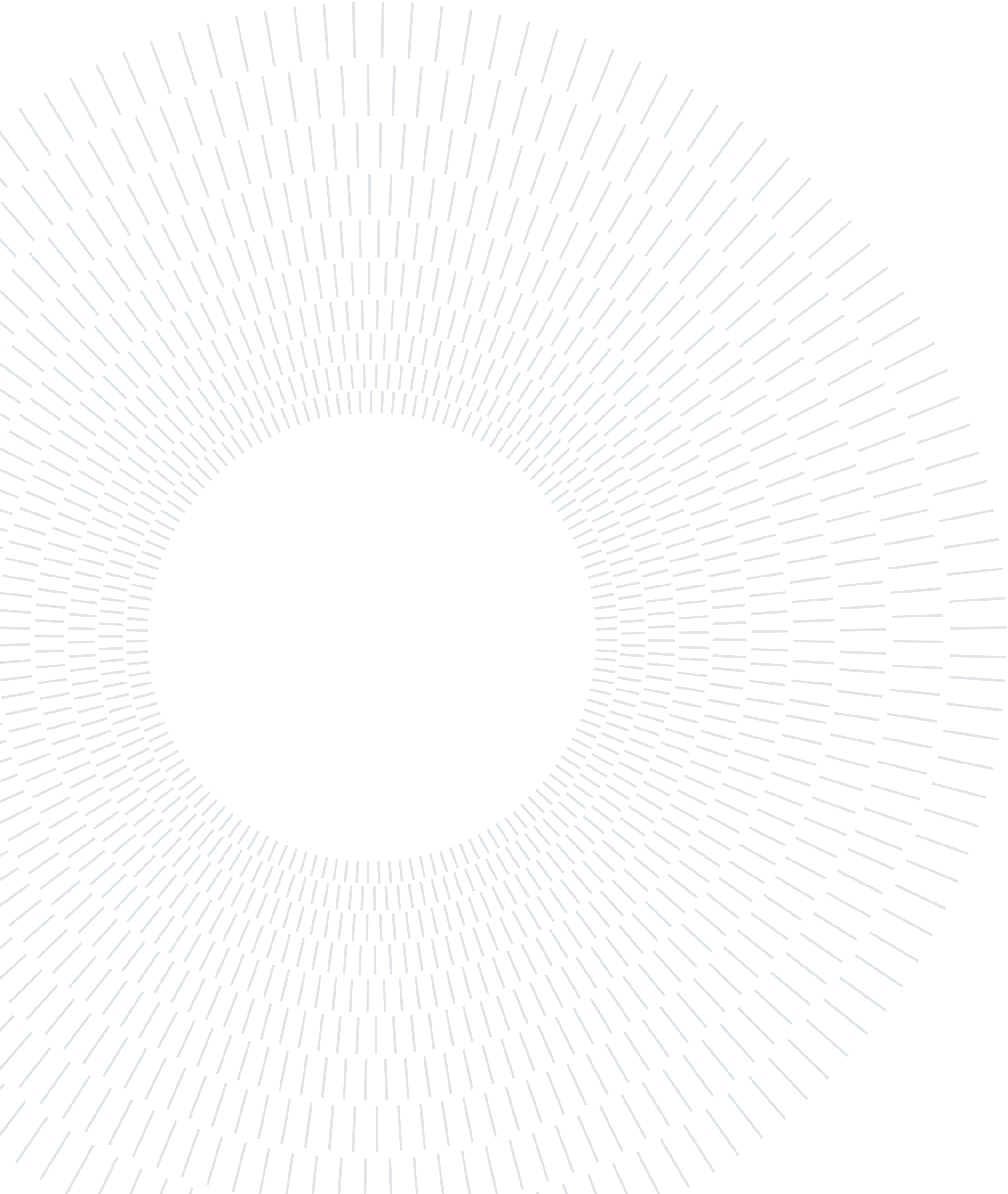

Acknowledgements

I want to thank Andrea, Alessia, Gianmaria, Giorgia, Teresa, Andrea Farina and Gianluca Valentini for all the help and opportunities they gave me. I will not forget physics department life!

Mamma, babbo, Niklas, Marta, Sangi and Giovanni have been indispensable moral support providers: grazie!